EM connectomics reveals axonal target variation in a sequence-generating network

Jörgen Kornfeld [1]†, Sam E. Benezra [2,3]†, Rajeevan T. Narayanan [4,5], Fabian Svara [1], Robert Egger [2,3], Marcel Oberlaender [4,5], Winfried Denk [1], and Michael A. Long [2,3]*

[1] Max Planck Institute of Neurobiology, 82152, Martinsried, Germany

[2] NYU Neuroscience Institute and Department of Otolaryngology, New York University Langone Medical Center, 10016, New York, NY, USA

[3] Center for Neural Science, New York University, 10003, New York, NY, USA

[4] Computational Neuroanatomy Group, Max Planck Institute for Biological Cybernetics, 72076 Tübingen, Germany

[5] Bernstein Center for Computational Neuroscience, 72076, Tübingen, Germany

*Correspondence to: mlong@med.nyu.edu

†Authors contributed equally to this work

The sequential activation of neurons has been observed in various areas of the brain, but in no case is the underlying network structure well understood. Here we examined the circuit anatomy of zebra finch HVC, a cortical region that generates sequences underlying the temporal progression of the song. We combined serial block-face electron microscopy with light microscopy to determine the cell types targeted by $HVC_{(RA)}$ neurons, which control song timing. Close to their soma, axons almost exclusively targeted inhibitory interneurons, consistent with what had been found with electrical recordings from pairs of cells. Conversely, far from the soma the targets were mostly other excitatory neurons, about half of these being other $HVC_{(RA)}$ cells. Both observations are consistent with the notion that the neural sequences that pace the song are generated by global synaptic chains in HVC embedded within local inhibitory networks.

INTRODUCTION

Neural sequences are central to many models of circuit function (Diesmann, Gewaltig et al. 1999, Jin, Ramazanoglu et al. 2007, Gibb, Gentner et al. 2009, Fiete, Senn et al. 2010, Mostafa and Indiveri 2014, Cannon, Kopell et al. 2015, Rajan, Harvey et al. 2016), and neurons often fire sequentially during specific behaviors (Hahnloser, Kozhevnikov et al. 2002, Peters, Chen et al. 2014, Mello, Soares et al. 2015) or cognitive states (Pastalkova, Itskov et al. 2008, Harvey, Coen et al. 2012), but the network properties that underlie such dynamics are poorly understood. Here we explore the synaptic connections within the zebra finch HVC, which is central to generating the neuronal activity necessary to coordinate activation of vocal muscles during the highly reproducible courtship song (Nottebohm, Stokes et al. 1976, Vu, Mazurek et al. 1994, Aronov, Andalman et al. 2008, Long and Fee 2008). Song progression is paced by $HVC_{(RA)}$ neurons, which project to the primary downstream target area, known as the robust nucleus of the arcopallium (RA) (**Figure 1a**). During the song, an $HVC_{(RA)}$ neuron is either silent

or active in the form of a burst of action potentials that occurs at a single precise and cell-specific time (Hahnloser, Kozhevnikov et al. 2002, Kozhevnikov and Fee 2007, Long, Jin et al. 2010, Vallentin and Long 2015). At any moment, it is estimated that about 200 of these 'pacer' neurons are active and can drive the appropriate motor activity (Fee, Kozhevnikov et al. 2004), presumably through a set of specific synaptic connections in RA (Fee, Kozhevnikov et al. 2004, Markowitz, Liberti et al. 2015, Lynch, Okubo et al. 2016, Picardo, Merel et al. 2016).

It has been difficult to discriminate between different models of sequence generation in HVC, in part because of the unknown connectivity within that nucleus. One class of models uses a synaptic (or 'synfire') chain architecture (Amari 1972, Abeles 1991, Diesmann, Gewaltig et al. 1999), which can deliver highly reliable and precise timing but requires direct connections between the pacer neurons (Li and Greenside 2006, Jin, Ramazanoglu et al. 2007, Long, Jin et al. 2010, Cannon, Kopell et al. 2015). Such connections are, however, only rarely seen with paired intracellular recordings, which at the same time showed that $HVC_{(RA)}$ neurons are connected with high probability (> 0.50) to nearby inhibitory interneurons (Mooney and Prather 2005, Kosche, Vallentin et al. 2015). This observation weakened the case for synfire chain-based sequence generation in HVC and sparked the development of alternative hypotheses that do not require direct connections between excitatory cells (Yildiz and Kiebel 2011, Hamaguchi and Mooney 2012, Amador, Perl et al. 2013, Goldin, Alonso et al. 2013, Armstrong and Abarbanel 2016, Hamaguchi, Tanaka et al. 2016, Rajan, Harvey et al. 2016). There are, however, a number of reasons paired recordings may fail to correctly estimate the connection rate between excitatory cells, among them the severing of axons during slice preparation (Stepanyants, Martinez et al. 2009) and an oversampling of closely spaced neurons (Jiang, Shen et al. 2015). To avoid this bias, we used a structural approach combining anatomical reconstructions of complete cells in light microscopy (LM) with high-throughput serial block-face electron microscopy (SBEM) (Denk and Horstmann 2004, Seung 2009).

RESULTS

We used both LM and EM, because anatomically, synapses can only be identified unambiguously in EM, but currently the size of the volume that can be studied by EM is limited to several hundred microns in one dimension (Helmstaedter 2013). This size is too small to explore the full extent of HVC connectivity, given that axon collaterals of HVC neurons ramify widely throughout the nucleus (e.g. **Figure 1—figure supplement 2a**), which is roughly 2000 x 500 x 500 μm^3 in size (Nixdorf-Bergweiler and Bischof 2007). We therefore used LM to explore the mesoscale structure of the axonal morphology and EM to analyze synaptic connectivity. To identify $HVC_{(RA)}$ cells, we injected markers into RA that are retrogradely transported, fluorescent Tetramethylrhodamine (TMR, also called fluoro-Ruby) or biotinylated dextran (BDA, **Figure 1—figure supplement 1**), for tissue to be observed in LM or EM, respectively.

To enable the LM-based reconstruction of the entire dendrite and of the axonal collaterals within HVC for single $HVC_{(RA)}$ cells, we used *in vivo* two-photon microscopy to target (Komai, Denk et al. 2006) TMR-labeled somata for Neurobiotin labeling (**Figure 1b**). We eliminated all cells (29 of 44) where the labeling intensity varied between different parts of the neurite or where no descending axon could be found. The remaining 15 cells were imaged at 92 x 92 x 500 nm^3 voxel size using a transmitted light brightfield microscope (Oberlaender, Bruno et al. 2007) and reconstructed using Neuromorph (see Methods) (**Figure 1c**,**d, Figure 1—figure supplement 1a-e; Video 1**). In agreement with other observations (Dutar, Vu et al. 1998, Mooney 2000, Kosche, Vallentin et al. 2015), we found that $HVC_{(RA)}$ dendrites were compact, with 95.0 ± 2.0% (SEM) of the dendritic path found within 100 µm of the soma (**Figure 1e**). In contrast, the axon collaterals, which were lined with synaptic boutons throughout (**Figure 1—figure supplement 2b**), ramified across HVC. For each cell (n = 15), the dendrite was entirely (100%) confined to

HVC, while the axon (with the exception of the branch projecting to RA) was also largely restricted to the boundaries of HVC (97% on average).

To quantify the prevalence of different types of synaptic inputs onto the dendrite of $HVC_{(RA)}$ cells, we next acquired a SBEM data set (166 x 166 x 77 μm^3 overall size, comprising 15104 x 15104 x 2661 voxels, each 11 x 11 x 29 nm^3 in size) from the central part of HVC (**Figure 1f, Figure 1—figure supplement 1f-j**, **Videos 2 and 3**). All raw data as well as skeletonized reconstructions are available online (Kornfeld 2017) (https://github.com/jmrk84/HVC_paper). Within this volume, 34 somata were positively identified as $HVC_{(RA)}$ neurons by the presence of a BDA-derived electron density (**Figure 1f**). This number is approximately 14% of the expected value of $HVC_{(RA)}$ somata (240 ± 28, SEM), given that there are about 40,000 ± 3,800 (SEM) $HVC_{(RA)}$ cells (Wang, Hurley et al. 2002) and the total HVC volume is 0.35 ± 0.024 mm^3 (n=14, SEM). For 12 of the 34 labeled $HVC_{(RA)}$ neurons, we manually reconstructed (skeletonized) (Helmstaedter, Briggman et al. 2011) the dendrite as far as possible. These reconstructions ranged in dendritic path length from 642 µm to 1956 µm (1290 ± 469 µm, mean ± SD) compared with complete LM-based reconstructions (1438 µm to 4819 µm, mean ± SD: 3187 ± 997 µm). Although ~70% (174 out of 248) of dendritic branches reached the boundary of the EM data set and were thus incomplete, 74 branches were completely reconstructed, including their most distal inputs (median ± SD of maximum soma distances: 90.9 ± 8.6 µm and 116.7 ± 29.4 for EM and LM, respectively). Our reconstructions therefore sample the full gamut of input types. While we do not find any variation of the input type with dendritic distance from the soma beyond a distance of 40 microns (see below), it cannot be completely ruled out that a subtle bias exists that lies below our detection threshold but might be discoverable when using larger data volumes.

We started by classifying for one cell all (1,003) incoming synapses (**Figure 1g-h**) by visually inspecting their ultrastructural details (Gray 1959, Colonnier 1968) (**Video 4 and 5**). We found that 396 (39.5%) synapses were asymmetric and thus presumably excitatory, and 607 (60.5%) were symmetric (inhibitory) cases. If it was not possible to classify a synapse based on its inspection directly, additional synapses nearby on the same axon were analyzed, since it can be assumed that they are of the same type (Eccles 1976) (**Figure 1—figure supplement 3**). Our synapse classification is reliable: in 19 out of 20 randomly selected test cases, a 2nd expert independently came to the same conclusion and in another set of test cases (8 $HVC_{(RA)}$, 11 $HVC_{(X)}$, and 31 interneuron synapses), where the neuron type was known based on somatic and dendritic morphology (**Figure 2d, Figure 2 – figure supplement 1**), all synapses were correctly classified by an expert unaware of the cell type.

The dominance of inhibitory synaptic inputs was consistently observed for $HVC_{(RA)}$ cells: when we applied our synapse classification procedure to 97 short dendritic stretches (first and third quartile of stretch length: 13.3 µm and 21.6 µm) randomly selected from 8 of the other skeletonized $HVC_{(RA)}$ cells, we found that across neurons the average ratio between excitatory and inhibitory synapses was statistically indistinguishable ($p = 0.36$, one-way ANOVA) from that found in the completely analyzed neuron. Inhibitory synapses were significantly enriched near the soma (68 ± 4% of all synapses at most 40 µm from the soma are inhibitory compared to 57 ± 2%, for synapses beyond that distance, mean ± SEM, $p < 0.05$, Wilcoxon rank-sum test, **Figure 1i**), an observation also made in cortical neurons (Anderson, Douglas et al. 1994). To estimate the number of excitatory and inhibitory synapses that a single $HVC_{(RA)}$ neuron receives on average, we first calculated dendritic synapse densities for all 9 analyzed cells separately for asymmetric (0.25 ± 0.02 µm^{-1}, mean ± SEM) and for symmetric synapses (0.36 ± 0.02 µm^{-1}). To get expected counts per cell, we multiplied these with the full dendritic path length (on average 3.2 mm per neuron), determined from LM reconstructions. Thus, on average well above half of

158 all synapses onto $HVC_{(RA)}$ dendrites are symmetric (59%, 1144 ± 429, mean ± SD) and only
159 41% are asymmetric (786 ± 311) — a surprising dominance of inhibitory inputs that stands in
160 stark contrast to mammalian cortical neurons (Beaulieu, Kisvarday et al. 1992, Peters 2002,
161 Kasthuri, Hayworth et al. 2015), where the inhibitory synapses are typically found to be at most
162 20% of the total.
163
164 We next inspected all BDA-labeled dendrites emerging from the 12 aforementioned cells for
165 synapses in which the presynaptic axon was labeled, and thus had to come from other $HVC_{(RA)}$
166 cells (**Figure 1j**). We found 44 such homotypic synapses between $HVC_{(RA)}$ cells (see Methods),
167 but they comprise only about 1% among an estimated total of 3,817 ± 926 (SD) incoming
168 excitatory synapses. Their median size (0.21 μm^2) and size variation (first and third quartile:
169 0.10 μm^2 and 0.48 μm^2), were statistically indistinguishable from those for all asymmetric
170 synapses (0.17 μm^2; first and third quartile: 0.08 μm^2 and 0.39 μm^2, $p > 0.05$, Wilcoxon rank-
171 sum test, **Figure 1k**). One might be tempted to consider the small number of double-labeled
172 synapses as evidence that $HVC_{(RA)}$-$HVC_{(RA)}$ connections are rare. However, BDA labeled only a
173 small fraction ($1/7^{th}$) of all $HVC_{(RA)}$ cells in our data set (**Figure 1—figure supplement 4a**) and
174 even for those, axonal collaterals were often incompletely filled (**Figure 1—figure supplement**
175 **4b**), suggesting the probability that a given stretch of $HVC_{(RA)}$ axon is labeled could be quite
176 small. To estimate this probability, we created a 300-member set of 1 μm^3 cubes randomly
177 placed throughout the SBEM volume and measured the total labeled axonal path length they
178 contained. The value obtained (38.6 µm of labeled axon across 300 cubes) is about 13 times
179 smaller than that expected given an estimate of the combined axonal path length (585.6 m) of
180 all 40,000 $HVC_{(RA)}$ cells. The axonal labeling probability of 7.6 ± 1.6% (SEM, see Methods) in
181 turn implies that the homotypic $HVC_{(RA)}$ synapses constitute ~15 ± 4% (SEM) of all excitatory
182 synapses onto $HVC_{(RA)}$ neurons.
183

We next took a presynaptic perspective to independently estimate the extent of $HVC_{(RA)}$-$HVC_{(RA)}$ connectivity and used a transsynaptic tracing scheme (McGuire, Gilbert et al. 1991) to determine the cell-type of the targets of the outgoing synapses on BDA-labeled axon collaterals (**Figure 2a**). The three main cell types found in HVC (Dutar, Vu et al. 1998, Kubota and Taniguchi 1998, Mooney 2000) are easily distinguished in LM: Inhibitory interneurons have smooth dendrites with a nearly complete lack of spines (Mooney 2000, Wild, Williams et al. 2005), and excitatory neurons project to either RA or to the basal ganglia (Area X), with the descending axon clearly recognizable. Even short stretches of dendrite can be reliably ascribed to one of the three types, because the spine density varies widely between but not within them (Dutar, Vu et al. 1998, Kubota and Taniguchi 1998, Mooney 2000) (**Figure 2b,c**). Dendrites were largely aspinous (0.01 ± 0.01 spines/µm, mean ± SD) for interneurons, densely covered with spines (0.70 ± 0.13 spines/µm) for $HVC_{(X)}$ cells and less so (0.21 ± 0.07 spines/µm) for $HVC_{(RA)}$ neurons. This spine density metric correctly classified 17 out of 18 BDA-labeled $HVC_{(RA)}$ dendrites in EM as well as 11 inhibitory neurons that had been classified using other morphological characteristics (symmetric synapses and a large soma diameter, **Figure 2—figure supplement 1a**). We used this to classify the cell type of postsynaptic dendritic segments (n = 528) transsynaptically traced from 9 BDA-labeled axons fully reconstructed in the EM volume. In 41 of 569 cases, the cell type could not be determined. These cases were excluded from further analysis, because the ultrastructure was obstructed by the BDA label (n = 33) or because the recovered dendritic branch was too short (n = 8), see Methods, **Figure 2d**.

When we examined three BDA-stained axons that each emerged from labeled somata in the SBEM dataset (path lengths: 1.37, 0.88, and 0.72 mm), we found that of 121 connections, 115 terminated on dendrites of inhibitory cells but only 6 onto excitatory cells, 4 of which being other $HVC_{(RA)}$ cells (e.g., **Figure 2e**). This agrees with the high connectivity found for closely spaced $HVC_{(RA)}$-interneuron pairs by electrical recordings (Kosche, Vallentin et al. 2015) as well as with

reports using EM connectomics for other cortical tissue (Bock, Lee et al. 2011). However, at this density, there would only be about 20 homotypic synapses per $HVC_{(RA)}$ neuron, which is about 6 times smaller than our estimate derived from the BDA-labeled inputs onto $HVC_{(RA)}$ dendrites.

We then examined BDA-labeled axon fragments that were 'orphaned' (n=6, path length: 0.56 ± 0.27 mm, mean ± SD), i.e., could not be traced back to their soma and were therefore likely farther away from it. Three of the fragments were synaptically connected to one of the labeled dendrites and four were partially myelinated. We discovered that the prevalence of synapses onto excitatory neurons, and onto other $HVC_{(RA)}$ cells in particular, was much larger for orphaned fragments than for attached axons; increases were 13-fold ($HVC_{(RA)}$-E), from 5.0% (6 out of 121) to 64.6% (263 out of 407), and 11-fold ($HVC_{(RA)}$-$HVC_{(RA)}$), from 3.3% (4 out of 121) to 36.8% (150 out of 407) (**Figure 3a**). $HVC_{(RA)}$ dendrites were often connected by more than one synapse to a labeled axon (17 doubles, 3 triple, and 1 quintuple among 127 analyzed pairs). The much larger (compared to the proximal outputs) fraction of excitatory target cells for the orphans implies that the prevalence of the different target types must depend on the distance from the soma. This would also be consistent with the low connection probability of 0.7% between $HVC_{(RA)}$ cells found in electrophysiological recordings (Kosche, Vallentin et al. 2015), where the recorded somata are usually less than 200 µm apart (Mooney and Prather 2005, Jiang, Shen et al. 2015), while, as our LM reconstructions show, 56 ± 14% (SD) of the axon collaterals' path lies farther than 200 µm from the soma, with some of them ramifying over the extent of HVC (e.g., **Figure 1—figure supplement 2a**).

Can we estimate the distance of an orphan segment to its soma based on local information? It is apparent from our LM reconstructions that branching becomes less frequent as the distance from the soma increases (**Figure 3 b,c**). Consistent with this, $HVC_{(RA)}$ axons in the SBEM data set that were connected to a cell body were much more highly branched (12.4 ± 3.7, mean ±

SD, branch points/mm, **Figure 2e**) than most orphaned axon fragments, with an average of only 4.0 ± 4.3 (mean ± SD) branch points/mm. To obtain a quantitative estimate of the distance to the soma and its uncertainty based on the number of branch nodes on a branch and its length we used both a nearest neighbor (**Figure 3 d-g**) and a Bayesian (**Figure 3—figure supplement 1**) analysis (for details see Methods). We found that a synapse was much more likely to be connected to another $HVC_{(RA)}$ cell or to a $HVC_{(X)}$ neuron rather than to an inhibitory neuron if the synapse was farther away from the soma (**Figure 3d**). The transitions between these regimes may well be gradual: One of the orphaned axons (**Figure 3—figure supplement 2**) showed an unusually high branch density (11.4 branch points/mm), suggesting a location close to the soma (16^{th} to 84^{th} percentile: 35.8 to 72.3 µm and also made the majority of its connections (52 of 83, 63%) onto interneurons, twice the fraction seen for the other orphaned axons (32% ± 10%, mean ± SD).

To rule out the possibility that our findings are due to a selection bias, we estimated the fraction of homotypic synapses for the 59 BDA-labeled axon fragments found in the 300-member set (see above), tracing each fragment from the sampling cube until we found two synapses or reached the data set boundary, and determined the postsynaptic cell types. Out of 105 synapses, 65 targeted interneurons, 22 $HVC_{(X)}$ neurons, and 18 other $HVC_{(RA)}$ neurons. Since there are approximately 1111 ± 513 (SD) outgoing synapses inside HVC for each $HVC_{(RA)}$ neuron (given an axon path length of 14.7 mm and a total synapse density of 75.4 synapses/mm), we expect about ~191 ± 88 (SD) homotypic synapses per cell (on average, incoming and outgoing homotypic synapse have to be equal in number), comprising about a quarter (24 ± 4%, SEM) of all incoming excitatory synapses, and nearly half of all outgoing excitatory contacts. The discrepancy between the estimates of the homotypic fraction of incoming excitatory synapses from the dendritic (~15 %) and axonal perspective (~24 %) might

be due to the fact that when counting the number of double labeled synapses, we accepted only those where the labeling of the presynaptic terminal was unambiguous.

How can we be sure that all or at least most of the orphaned fragments belong to $HVC_{(RA)}$ neurons? Since BDA (which is transported in the retrograde direction much more efficiently than anterogradely in all tissues tested, including the zebra finch brain (Reiner, Veenman et al. 2000) was only injected into RA, any labeled axon has to belong to a cell with an axon that connects HVC and RA, as $HVC_{(RA)}$ axons do. If there is indeed a substantial number of cells in RA that project to HVC(Roberts, Klein et al. 2008), then it is possible that a substantial fraction of the orphaned axons could originate from those cells. To independently confirm the number of $RA_{(HVC)}$ cells, we injected the fluorescent tracer DiI (Invitrogen) into HVC, which heavily labeled the upstream nuclei NIf and Uva (**Figure 3—figure supplement 3**) but yielded only a small number of labeled somata in RA (125, 163, and 171, respectively, in three birds), approximately one for every 200 $HVC_{(RA)}$ neurons on average. To account for the density of labeled axon in our EM volume, each those cells would need a total axon path of ~4 m in HVC, which appears unlikely given that the extensively ramifying $HVC_{(RA)}$ axons have a length of only ~0.015 m.

DISCUSSION

We have shown that the synaptic architecture in HVC contains a density of connections between $HVC_{(RA)}$ neurons that might be sufficient to support a synaptic-chain model, whereby precisely timed sequences of action potential bursts in $HVC_{(RA)}$ neurons are generated by a wave of activity propagating via synaptic connections among these neurons without the need for inhibition-mediated propagation of activity (Yildiz and Kiebel 2011) or to involve structures outside HVC (Hamaguchi and Mooney 2012, Goldin, Alonso et al. 2013, Hamaguchi, Tanaka et al. 2016).

While we estimate that 25% of excitatory inputs to $HVC_{(RA)}$ neurons are homotypic, the sources of the remaining synapses are unknown. It should be a central goal of future efforts to quantify the relative number of connections from these regions (e.g., Uva, NIf, etc.) at the level of single $HVC_{(RA)}$ neurons. That said, many of these connections, such as auditory afferents (Vallentin and Long 2015), collaterals from $HVC_{(X)}$ neurons (Scharff, Kirn et al. 2000), and descending fibers from NIf are unlikely to play a role in motor patterning, since removal of NIf does not disrupt the song (Cardin, Raksin et al. 2005). The precise role of Uva, a thalamic region also directly projecting to HVC (Nottebohm, Kelley et al. 1982), remains to be determined (Coleman and Vu 2005, Hamaguchi, Tanaka et al. 2016).

Somewhat surprisingly, the low rates of pairwise connectivity seen in electrophysiological recordings (Mooney and Prather 2005, Kosche, Vallentin et al. 2015), which previously had been interpreted as evidence against a direct synaptic chain (Armstrong and Abarbanel 2016), are not inconsistent with our estimate that each $HVC_{(RA)}$ neuron receives a significant amount of its excitatory input from other $HVC_{(RA)}$ neurons. The reason is that with the around 200 homotypic inputs per cell, the probability to be connected to any one of around 40,000 $HVC_{(RA)}$ neurons can be at most 0.5%. The question remains what fraction of those inputs are true 'chain' synapses in that the presynaptic cell's activity immediately precedes that of the postsynaptic cell, but our study demonstrates that the anatomical substrate for the chain model exists.

An important next step will be to combine functional imaging with volume EM to directly test whether an $HVC_{(RA)}$ cell receives more numerous or stronger direct homotypic inputs from cells that fire immediately prior to its own activity. In fact, a recent study describes how calcium activity can be imaged in the singing bird (Picardo, Merel et al. 2016), a crucial step in that direction. One potential difficulty stems from our finding that $HVC_{(RA)}$ neurons preferentially form

distal connections, indicating that the timing circuitry in HVC is distributed and therefore requires a large EM volume (as much as 500 million μm^3, compared to 2 million μm^3 in our volume) for its complete reconstruction. It might take the better part of a year merely to acquire the raw data (Schalek, Lee et al. 2016). While even a few years ago it seemed impossible to analyze such an amount of data within a reasonable time frame, recent progress in the automation of segmentation are encouraging (Berning, Boergens et al. 2015, Januszewski, Maitin-Shepard et al. 2016, Beier, Pape et al. 2017, Dorkenwald, Schubert et al. 2017).

Our finding that connections near the soma are often onto inhibitory neurons suggests that inhibition plays an important role in sequence generation, which is further supported by the large overall fraction of inhibitory inputs. One function of those inhibitory connections could be to decorrelate excitatory activity in space and time: Not only are nearby $HVC_{(RA)}$ neurons rarely connected and thus unable to drive each other, but even when driven by a common input, only the cell(s) with the strongest input(s) will continue to fire in the face of the winner-take-all effect due to the strong reciprocal inhibition (**Figure 3h**). Winner-take-all behavior is normally associated with certain cognitive tasks (Hopfield and Tank 1985, Lundqvist, Rose et al. 2016), such as decision making (Usher and McClelland 2001). In HVC, it may help to prevent local clusters of activity, which could lead to leakage across different chains passing through adjacent excitatory neurons. An altogether different role for local inhibition may be the improvement of temporal precision by sharpening burst timing through recurrent inhibition (Hahnloser, Kozhevnikov et al. 2002, Long, Jin et al. 2010, Cannon, Kopell et al. 2015).

Inhibition may, furthermore, have a central role in shaping the distance dependency of postsynaptic targets during circuit development without the need for molecular cues (de Wit and Ghosh 2016). Instead, the architecture we observed may arise naturally from a pattern that initially follows Peters' rule (Braitenberg and Schüz 1998), which predicts synaptic connections

between cell types with intermingled axonal and dendritic arbors (Rees, Moradi et al. 2017), but is then refined as the interneurons increasingly prevent the co-activation of nearby excitatory cells, thereby destabilizing connections between them while leaving more distant connections intact. Such a preferentially distal connectivity would also favor more widely distributed synaptic chains, which could have the added benefit of relying more on axonal propagation delays for sequence timing (Budd, Kovacs et al. 2010). Overall, the observed synaptic architecture shows some resemblance with local inhibitory/excitatory networks linked by long-range excitatory/excitatory connections (coupled winner-take-all modules) that have been shown to make computational models of cortical sequence generation more robust (Binas, Rutishauser et al. 2014, Mostafa and Indiveri 2014).

MATERIALS AND METHODS

Animals

We used adult (>90 days post hatch) male zebra finches that were obtained from an outside breeder and maintained in a temperature- and humidity-controlled environment with a 12/12 hours light/dark schedule. All animal maintenance and experimental procedures were performed according to the guidelines established by the Institutional Animal Care and Use Committee at the New York University Langone Medical Center.

Surgery

To label only neurons that projected from HVC to the robust nucleus of the arcopallium (RA), we injected lysine-fixable retrograde dextran tracers (Invitrogen) conjugated to either Tetramethylrhodamine (fluoro-Ruby, mol. Weight: 10,000) or biotin (BDA, mol. weight: 3,000) for preparations to be inspected with light microscopy (LM) or electron microscopy (EM), respectively. We injected 200 nL of either Fluoro-Ruby (50 mg/mL) or BDA (100 mg/mL) into RA of anesthetized (1-3% isoflurane in oxygen) zebra finches using an injection system (Nanoject, Drummond Scientific) outfitted with a glass injection pipette (tip diameter: 30-40 μm). RA was

targeted using stereotaxic coordinates (2.30 mm lateral and 1.85 mm posterior from the midsagittal sinus) and success in finding the RA region was confirmed by observing characteristic spontaneous activity (Long and Fee 2008) using a carbon-fiber electrode (Carbostar-1, Kation Scientific) and an extracellular amplifier (NPI Electronic Instruments).

For *in vivo* imaging and dye loading, we first had to enable optical access to HVC. To accomplish this, a craniotomy (1 mm x 1 mm) was prepared over HVC. The underlying dura was then carefully removed with a flame sharpened tungsten wire (starting diameter: 0.5 mm). A small drop of saline buffer was applied to the exposed brain, followed by a 3 mm-diameter round cover glass (#0 thickness, Warner Instruments) as an optical window, which was first secured to the surrounding skull by applying light-curable acrylic (Flow-IT ALC; Pentron Clinical Technologies) around the edges of the glass. Dental acrylic (Cooralite Dental MFG) and cyanoacrylate were then added to permanently and stably attach the cover glass to the skull. A small metal head plate with two tapped holes was then implanted at the anterior part of the skull using dental acrylic for head fixation.

2-Photon Guided Cell Labeling

Juxtacellular labeling (Pinault 1996, Narayanan, Egger et al. 2015) with Neurobiotin (Vector Labs) was used to fill individual RA-projecting HVC ($HVC_{(RA)}$) neurons out of a population that had been retrogradely labeled from RA with fluoro-Ruby *in vivo*. After waiting at least 48 hours following the injection of the retrograde tracer into RA, two-photon imaging (Denk and Webb 1990) was used to identify the target cell and guide the pipette. On the day of single-cell labeling, a small pipette access hole (~400-500 µm) was drilled in the glass coverslip immediately lateral to the target recording region using a carbide bur drill bit (1/4 FG-100; Johnson-Promident). Glass pipettes were fabricated using a horizontal puller (P97, Sutter Instrument Company) and had a final resistance of 4-5 MΩ when loaded with internal solution

that consisted of 150mM K-Gluconate (Sigma) and 3% Neurobiotin. The microscope (MOM, Sutter Instrument Company) was of the moveable objective design (Euler, Hausselt et al. 2009) and was controlled using ScanImage (Pologruto, Sabatini et al. 2003) 3.8 with a 16x/0.8 NA water immersion objective (Nikon). Pipettes were made fluorescent either by adding 40 μM of Alexa 488 (Invitrogen) to the internal solution or by coating the pipette with green fluorescent quantum dots (Andrasfalvy, Galinanes et al. 2014). The activity of $HVC_{(RA)}$ neurons was recorded (IR-183, Cygnus Technology Inc), and cells were filled with Neurobiotin by applying 1000-1500 positive current pulses with an amplitude between 3 and 15 nA and a duration of 200 ms delivered at a frequency of 2.5 Hz.

Histological Procedures (LM)

Birds were anesthetized with pentobarbital sodium and perfused transcardially with 4% w/v paraformaldehyde (EMS) at least one hour after dye loading to permit adequate Neurobiotin diffusion. Brains were removed from the skull using a surgical scoop, immersed in 4% paraformaldehyde for 3-5 days to achieve thorough fixation, and incubated in phosphate buffer for an additional 1-3 days to decrease endogenous peroxidase activity. To prepare sections, the brain was cut across the midline, mounted on the sagittal surface with cyanoacrylate, and stabilized with 3% agarose. Parasagittal sections (100 μm thickness) of HVC were cut using a vibratome (Leica VT1000S). Slices were washed five times with phosphate buffer and treated with 3% H_2O_2 to further reduce endogenous peroxidase activity. Slices were then immersed overnight at 4°C in a solution containing avidin/biotin complexes and 0.5% Triton X-100 in phosphate buffer (Vector Labs and Sigma, respectively) to tag the Neurobiotin with peroxidase complex. On the following day, slices were washed 5 times with phosphate buffer and then immersed in a solution containing 2.3 mM diaminobenzidine (DAB, Sigma) and 0.01% H_2O_2 in phosphate buffer to label processes containing Neurobiotin. Slices were then washed and mounted on slides with Vectashield (Vector Labs) or Mowiol (Sigma-Aldrich) mounting medium.

To quantify the number of HVC-projecting RA neurons, we injected a retrograde tracer into HVC (DiI, Invitrogen D3911; 46 nL total injection volume) that labels neurons with high efficiency in zebra finches (Scott, Gardner et al. 2012). Following a two-day incubation period, animals were perfused with 4% paraformaldehyde, and 100 µm sagittal sections were cut across the entirety of RA, Nucleus Interfacialis (NIf), and nucleus Uvaeformis (Uva). Sections were mounted on slides using Vectashield (Vector Labs) and imaged with a confocal microscope (LSM 800, Zeiss; excitation / emission: 551 / 569 nm) using a 20x objective (0.8 NA). The z-stacks of retrogradely labeled $RA_{(HVC)}$ neurons were captured across the extent of RA, and the position of each cell was manually marked using the landmark function in Amira.

LM Imaging

Only well-filled $HVC_{(RA)}$ neurons were selected for reconstruction, specifically those in which the soma, dendrite, and axon were all labeled (even if faintly) without interruptions and with clearly labeled dendritic spines and presynaptic boutons were selected for high resolution LM imaging with a custom-designed high-resolution mosaic/optical-sectioning brightfield microscope system (Oberlaender, Bruno et al. 2007). In brief, a transmitted light brightfield microscope (Olympus BX51, Olympus, Japan), equipped with a motorized x-y-z stage (Maerzhaeuser, Wetzlar, Germany), a narrow bandpass (546 ± 5 nm) illumination filter and a 100x magnification oil-immersion objective (numerical aperture 1.4) was used to acquire image stacks from consecutive 100 µm thick brain sections. For each section, a 3D mosaic of images (e.g., 10 x 15 fields of view) covering the entire HVC was acquired at 92 x 92 nm pixel size and in steps of 500 nm mechanical defocus. Next we applied a linear image restoration algorithm (Tikhonow-Miller) using the Huygens software package (Scientific Volume Imaging, Netherlands). By inverting the gray values of the brightfield image stacks they could be treated as fluorescent data with an emission wavelength of 546 nm. The deconvolution used a point-spread-function

that takes the optical properties of biocytin-labeled brain tissue into account (Oberlaender, Broser et al. 2009). Deconvolved image stacks were then downsampled by a factor of 2 in x/y, yielding a final voxel size of 184 x 184 x 500 nm before axonal reconstruction. To quantify the bouton density, subvolumes that contained primarily horizontal (i.e. within the image plane) axonal branches were acquired at 200 nm focus increments and used without deconvolution.

Neuron reconstructions (LM)

Neuronal branches (dendrites and axons) were reconstructed in 3D using NeuroMorph (Oberlaender, Bruno et al. 2007). Automated tracing results from each histological section were manually proof-edited using FilamentEditor (Dercksen, Hege et al. 2014), custom-designed based on Amira visualization software (FEI-VisualizationSciencesGroup). In brief, maximum-intensity z-projections of the original image stacks were superimposed onto automatically generated 3D skeleton tracings of all putative neuronal branches contained within the imaged volume and segmented objects that had no correspondence in the projection image were manually deleted (Dercksen, Hege et al. 2014). Fragmented segments were spliced, and axonal branches were classified as ‘dendrite’ or ‘axon’ based on whether, respectively, spines or boutons were visible in the projection images. Whenever a neuronal branch reached one of the borders of the imaged volume, additional image stack regions were acquired that allowed us to follow the branch further. To account for shrinkage during histological processing, the reconstruction was scaled to match the thickness of 100 µm, as defined by the vibratome. The scaled 3D tracings from all consecutive sections were then combined and manually aligned using the FilamentEditor. The z-coordinate of each point was then replaced by the average of 9 points (the point itself and the 4 adjacent points in each direction) and resampled to a point spacing of about 1 µm. Smoothing in z and downsampling make path length measurements comparable to manual tracing results using Neurolucida Software (Microbrightfield). The NeuroMorph and FilamentEditor tools enable tracings that are independent of the experience of

the human operator, with an interuser-variability of approximately 20 µm per 1 mm axonal length(Dercksen, Hege et al. 2014). The borders of HVC were manually traced in each 100 µm tissue section using Neurolucida.

Analysis of LM reconstructions

The fraction of dendritic length contained within a certain distance of the soma was determined by conducting a spherical Sholl analysis (Sholl 1953) in Neurolucida (MBL sciences). The proportion of axonal pathlength both within HVC and within a 200 µm radius from the soma was computed in Amira for each neuron using the ZIB extension package (Egger, Dercksen et al. 2014). Axonal boutons and dendritic spines were annotated manually in Amira using high-resolution LM stacks. The location of each bouton or spine was marked in 3D and aligned in Amira to the corresponding branch reconstruction. Spine-densities were calculated for each branch by dividing its total spine count by its path length. Branch nodes (points where the axon bifurcates) were manually located in the reconstructions using Amira. Branch nodes for which one of the daughter branches was < 15 µm in length were not included in this analysis.

Histological Procedures (EM)

The bird used for the EM experiments was transcardially perfused in a way that preserves the extracellular space and leads to minimal shrinkage (JK, unpublished observations), by using high pressure and the following fixative solution: 0.07 M sodium cacodylate (Serva), 140 M sucrose (Sigma), 2 mM $CaCl_2$ (Sigma) with 2% paraformaldehyde and 2% glutaraldehyde (Serva) added (Cragg 1980). The brain was removed and, using a vibratome (Leica VT1000S), cut into slices each about 200 µm thick. One of the slabs that centrally intersected HVC was selected and post-fixed in the same solution overnight, rinsed several times with cacodylate buffer and permeabilized in a 30% sucrose solution by exposing it to one freeze-thaw cycle in liquid nitrogen. Residual peroxidase activity was suppressed by soaking the sample in 3% H_2O_2

for 30 minutes before labeling the sample with an avidin-peroxidase complex and DAB, as described in a previous section. The sample was then rinsed several times in cacodylate buffer. Heavy metal staining was added through a conventional ROTO protocol using the following steps interspersed with rinses in cacodylate buffer (after first Osmium step) or H_2O (all others): 2% OsO_4 (Serva), reduced with 2.5 % potassium hexacyanoferrate(II) (Sigma) 2 h, room temperature; 1% thiocarbohydrazide in H_2O, 1 h, 58 °C (Sigma); 2 % OsO_4, 2 h; 1.5 % uranyl-acetate in H_2O, 53°C (Serva); 20 mM lead-aspartate, 2 h, 53°C (Sigma) (Seligman, Wasserkrug et al. 1966, Karnovsky 1971, Walton 1979). Dehydration was performed using an ethanol series with 10, 15, 10, 10 minutes at 70%, 100%, 100%, and 100% ethanol (Electron Microscopy Sciences). The sample was infiltrated with epoxy monomer (epon hard, Serva) (Glauert and Lewis 2014) dissolved in propylene oxide (Sigma) for 3 h and for 3 h with pure monomer before final embedding and curing (48 h at 60°C). The sample was then trimmed and glued with epoxy to a custom-made aluminum holder and trimmed into a pyramidal-shape before gold coating for better conductivity.

SBEM Imaging and data preprocessing

We performed serial block-face electron microscopy (Denk and Horstmann 2004) at 11 × 11 × 29 nm voxel size using a scanning electron microscope with a field-emission cathode (UltraPlus, Zeiss, Oberkochen, Germany) equipped with a custom-built in-chamber microtome in high-vacuum (raw and effective voxel rates were 5 and 2.1 MHz respectively) at a dose of 10.3 electrons/nm^2, 2 kV landing energy with a custom back-scatter electron detector and amplification system optimized for fast acquisition speeds. Before each cut, a subregion of the block face was imaged using four overlapping micrographs resulting in an image stack. Images were registered by affine transformations (https://github.com/billkarsh/Alignment_Projects) (Scheffer, Karsh et al. 2013, Karsh 2016) and converted to a KNOSSOS (www.knossostool.org)

data set for reconstruction and browsing with custom Python code (https://github.com/knossos-project/knossos_python_tools/tree/master/knossos_cuber) (Kornfeld 2017).

Neuron reconstructions (EM)

Each annotator received at least 10 hours of training and was considered an expert after one year of annotation experience. BDA-labeled neurons, using the soma as a starting place, were skeletonized within the EM stack in KNOSSOS by an expert annotator, and errors were corrected by the same individual in a second pass, which was also used for synapse annotation. All BDA-labeled axons, including orphaned axons, were traced by at least two independent annotators and discrepancies were resolved by an expert that had not participated in the initial annotation. Synapses on each axon were then labeled (see synapse identification) and proofread by an expert annotator who excluded cases where the BDA-label obscured the ultrastructure. The remaining synapses were used to seed the tracing of the postsynaptic dendrite segment. Annotators were instructed to reconstruct the postsynaptic dendrite to the end of the branch in one direction and to the next main branch point in the other direction. All dendritic-branch tracings were proofread by an expert and only included if at least a minimum path length of 10 µm could be reconstructed. All EM reconstructions were analyzed and visualized with custom Python code using the Mayavi2 (Enthought) library (Kornfeld 2017, Kornfeld 2017).

EM synapse annotation

Synapses were labeled by an expert annotator and classified as symmetric or asymmetric (**Video 4 and 5, Figure 1—figure supplement 3**). Active-zone ’diameters‘ were quantified by measuring - with KNOSSOS - the cross-sectional length of the synaptic thickening in that plane and principal viewing orientation (x, y, or z) in which the contact cross section appeared largest. Diameters were then converted to areas by assuming a circular synaptic contact.

Classification of postsynaptic cell type

To estimate dendritic spine density, a stretch of the postsynaptic dendrite (> 10 µm) was selected that often included the place where the axon was in contact with the dendrite. We counted as a spine every skeleton branch with a length greater than 1 µm that emerged from the dendritic shaft. Some postsynaptic protrusions found on interneurons contained multiple synapses (e.g., **Figure 2—figure supplement 1b**). Therefore, spines were defined as receiving no more than one synapse at their ends by three independent annotators. The resulting spine density D_{spine} (in μm^{-1}) was used to classify the dendritic stretch as belonging to an interneuron ($D_{spine} < 0.11$), $HVC_{(RA)}$ ($0.11 < D_{spine} < 0.46$), or $HVC_{(X)}$ neuron ($0.46 < D_{spine}$). To detect dendritic reconstructions that were traced from separate synapses but belonged to the same dendrite, we detected overlap between skeletons using the following criterion: a node was considered to overlap another skeleton if it was less the 400 nm from any edge of all other skeletons. Dendritic reconstructions were defined as belonging to the same neuron when at least 25% of their nodes overlapped. Since the postsynaptic dendritic reconstructions were never complete (i.e. only parts of the entire neuron could be reconstructed), our analysis could only positively identify reconstructions as belonging to the same cell. For dendrites that were found to belong to the same cell (grouped together after being traced from different synapses), spine density was averaged before classification.

Estimating the axon-to-soma distance

We used two different ways to estimate the distance between an orphaned branch and its soma from its number of branch nodes inside the EM volume, both based on the LM observation that the density of branch nodes, D_b, varies with soma distance (r) (**Figure 3c**). The first way used a Bayesian approach to calculate the probability distribution over r, given a branch of length *l* and

a branch-node count of *N* (**Figure 3c**), which can be used to estimate, as needed, mean, median, variance or any quantile for r:

$$P(r|N,l) \propto P(N,l|r) * \mathrm{P}_a(r),$$

whereby

$$P(N,l|r) = \frac{(\mathrm{D}_b(r)*l)^N * e^{-D_b(r)*l}}{N!},$$

which assumes that the branch nodes are placed independently from each other and are, therefore, Poisson distributed with a node-count expectation value of $\lambda = D_b(r) * l$. Fitting the LM measurements to an exponential gave $D_b(r) = (35.448 * e^{-\frac{r}{43.5mm}} + 0.613)/\mathrm{mm}$. The Bayesian prior, $P_a(r)$, i.e. the probability that an axon segment is found at a distance between r and r±Δ from its soma, was estimated by applying Gaussian kernel density estimation (Python scipy.stats.gaussian_kde, scott bandwidth selector) to the LM based axon distribution measurements.

The other way to relate r to N and l is to sample the LM data directly: We divided each of the 15 LM stacks into volumes shaped identically to the EM volume and recorded for each volume and for all contained orphaned branches their lengths, distances from the soma, and branch-node counts. Only branches that both entered and left the sampled subvolume were considered (about 95% of the total) because all of the reconstructed orphaned branches in the EM volume also had that property. This was repeated with the origin of the division grid shifted in 10 µm increments along all 3 axes resulting in 17 × 17 × 8 different divisions for each LM stack. For a given orphaned branch in the EM volume, we selected all those sample branches that had the

same node count and a length within ± 10%. The distribution of their soma distances was then used in the same way as the probability distribution coming from the Bayesian approach.

Estimating the fraction of homotypic $HVC_{(RA)}$ synapses

In order to estimate the homotypic fraction of all excitatory synapses onto $HVC_{(RA)}$ cells, we determined the density of homotypic synapses by counting the number of double labeled synapses and correcting it for the axonal labeling efficiency. Labeling efficiency was estimated by comparing the volume density of labeled axon length by inspecting 300 randomly placed 1 μm^3 cubes with the density expected for $HVC_{(RA)}$ neurons using published estimates for their total number (Wang, Hurley et al. 2002) and the average axonal path length from LM reconstructions. To count the number of double labeled synapses, BDA-labeled dendrites were searched by an expert annotator for synapses with labeled axons by following them in KNOSSOS at the full voxel resolution, instructed to annotate also synapses with weak labeling. The found synapses were then scrutinized by JK and the result was confirmed by ML and SB.

All error estimates were calculated assuming independence of the errors using the variance formula for error propagation.

Acknowledgments

This research was supported by the National Institutes of Health (Grant R01NS075044) (M.A.L.) and (F31 NS084767) (S.E.B.), the New York Stem Cell Foundation (M.A.L.), the Max Planck Society (J.K., F.S. R.T.N., M.O., W.D), the Bernstein Center for Computational Neuroscience, Boehringer Ingelheim Foundation (J.K., F.S.), the German Federal Ministry of Education and Research Grant BMBF/FKZ 01GQ1002 (M.O.), and the European Research Council (M.O.) under the European Union's Horizon 2020 research and innovation program (grant agreement No. 633428). We thank L. Gibb, M. Halassa, D. Jin, K. Katlowitz, G. Kosche, M. Picardo A. Reyes, D. Rinberg, R. Tremblay, and D. Vallentin for comments on the manuscript. We are grateful to A. Al-Shaboti, A. Andrade Garcia, E. Atsiatorme, D. Baltissen, S. Bassler, F. Bassler, J. Bessler, D. Dimitrov, M. Ederer, T. Eliguezel, O. Fedorashko, L. Fey, J. Foehr, A. Gaubatz, S. Gottwalt, M. Gross, J. Hammerich, L. Hammes, H. Hees, J. Hendricks, J. Huether, S. Hutzl, R. Janssen, K. Kappler, F. Kaufhold, K. Kehrle, K. Kiesl, J. Kupke, J. Loeffler, S. Mertens, O. Mueller, T. Noel, L. Obenauer, G. Patzer, J. Pellegrino, D. Raica, C. Sandhof, M. Schramm, J. Schwab, D. Schwarz, J. Serwani, A. Sons, J. Tytko, D. Wachmann, and S. Zaschke for help with EM data analysis, J. Kuhl for help with figure preparation, and J. Tritthardt for building custom electronics.

Figure Legends

Figure 1 Analysis of synaptic inputs onto $HVC_{(RA)}$ dendrites. (**a**) A schematic of the songbird brain showing HVC and its two main downstream targets, RA and Area X. (**b**) A backlabeled $HVC_{(RA)}$ neuron (red) during juxtacellular filling (pipette shown in white) guided by 2-photon imaging of fluoro-Ruby. (**c**,**d**) A Neurobiotin-filled cell from (**b**) in brightfield LM after histochemical processing (**c**) and dendritic reconstruction (**d**). (**e**) Normalized count of dendritic path length vs. soma distance for 15 $HVC_{(RA)}$ neurons; individual cells (gray) and average (red). Bin size: 10µm. (**f**) Cross-section through a SBEM stack showing BDA-labeled $HVC_{(RA)}$ somata. (**g**) Inhibitory (blue spheres) and excitatory (gold spheres) synapses onto an $HVC_{(RA)}$ dendrite in the SBEM volume. Sphere cross-sectional areas are proportional to the active zone area. (**h**) Higher magnification of a dendritic branch from (**g**). (**i**) Density of asymmetric and symmetric synapses vs. the distance to the soma. (**j**) Two $HVC_{(RA)}$ dendrites; red spheres indicate double-labeled synapses, with cross sections through two synapses (insets). Inset, cross sections through the synapses circled in red. (**k**) Active zone size distributions of inhibitory (blue), excitatory (black), and double-labeled (red) synapses. Scale bars are 10 µm in b and c, 25 µm in f, and 0.25 µm in j.

Figure 1—figure supplement 1. Sample preparation for LM and EM. (**a,b**) For LM, $HVC_{(RA)}$ neurons are retrogradely labeled by injecting a fluorescent dextran (fluoro-Ruby) into RA (**a**), and a single labeled neuron is targeted and filled with Neurobiotin under the guidance of 2-

photon microscopy (**b**). (**c**) The tissue is then fixed and 100 µm parasagittal sections are sliced through the entirety of HVC. (**d**,**e**) Sections are further processed to stain Neurobiotin-labeled neurites (**d**) and then imaged in brightfield with a 100x objective (**e**). (**f**) For EM, $HVC_{(RA)}$ neurons are retrogradely labeled with biotinylated dextran (BDA). (**g,h**) A single 200 µm parasagittal section is taken from the center of HVC (**g**) and further processed to stain BDA-labeled neurites (**h**). (**i**,**j**) A cube of tissue from within the center of HVC is extracted and stained by ROTO (reduced osmium OTO) (**i**) before being imaged via SBEM (**j**).

Figure 1—figure supplement 2. Synaptic boutons on $HVC_{(RA)}$ axon collaterals. (a) An LM reconstruction of $HVC_{(RA)}$ axon collaterals of one neuron with the HVC border indicated by dashed lines. Locations of all synaptic boutons are marked by grey spheres. **(b)** Bouton density of collateral branches as a function of their midpoint distances from the soma.

Figure 1—figure supplement 3. Ultrastructural classification of synapses. (**a**) An asymmetric synapse onto a BDA-labeled $HVC_{(RA)}$ dendrite whose morphology is partially obscured by the label. Red arrows indicate the synaptic cleft. (**b** to **d**) Other synapses made by the same axon onto unlabeled dendrites. The pronounced postsynaptic density (PSD), especially for synapse 4, confirms the classification of this connection as excitatory. (**e**) A symmetric synapse onto a BDA-labeled $HVC_{(RA)}$ dendrite. (**f** to **h**) Synapses from the same neuron onto other unlabeled dendrites display a lack of a PSD and a different appearance of synaptic vesicles compared with the asymmetric synapses. Scale bar: 0.5 µm.

Figure 1—figure supplement 4. The BDA label is inefficient and incomplete. (**a**) All cells within our SBEM dataset are represented by spheres at the location of the cell body. Known $HVC_{(RA)}$ neurons, which were labeled with BDA, were colored red. Also shown are putative $HVC_{(RA)}$ neurons, classified by morphological features of the soma and dendrite (pink), other neuron types (large gray spheres), and glia (small gray spheres). Scale bar: 50 µm. (**b**) Incomplete labeling of axonal collaterals of $HVC_{(RA)}$ neurons inside HVC is demonstrated with a skeleton reconstruction (labeled axon in black and unlabeled axon in gray). The inset electron micrographs correspond to the portions of the axonal field indicated. Scale bars: left: 1 µm, right: 5 µm.

Figure 2 Classification of postsynaptic targets. (**a**) A BDA-labeled axon with 4 synaptic boutons (boxes). One bouton and its postsynaptic structure labeled in red and blue, respectively: In cross section (top right) and as a surface reconstruction (bottom center). (**b**) Dendrites from an inhibitory interneuron, an $HVC_{(RA)}$ neuron, and an $HVC_{(X)}$ neuron (left to right) in LM. Spine locations are indicated by grey spheres. (**c**,**d**) Spine densities for each of these neuron classes from LM (**c**) and EM (**d**) reconstructions. Insets show examples with spines indicated by arrowheads. (**e**) SBEM-based reconstructions of two $HVC_{(RA)}$ somata with their proximal axons. Blue, green, and red spheres mark the location of synapses with inhibitory interneurons, $HVC_{(RA)}$ neurons, and $HVC_{(X)}$ neurons, respectively. Scale bar is 0.25 µm in a.

Figure 2—figure supplement 1. Morphological markers of interneurons. (**a**) Ultrastructural and morphological differences of the somata of an HVC interneuron (left, blue shade) and an $HVC_{(RA)}$ neuron (right, red shade). Compared with $HVC_{(RA)}$ neurons, interneurons had large amounts of endoplasmatic reticulum (ER), many mitochondria, and a large cell body. Scale bar: 7.5 µm. (**b**) An electron micrograph (cut plane rotated to show spine attached to dendrite) showing a polysynaptic protrusion (blue label) that receives four synapses at its tip, that was previously misclassified as a dendritic spine of an excitatory cell. The four presynaptic axons are colored in yellow, green, purple and red. Scale bar: 1 µm.

Figure 3 Spatial variation of postsynaptic cell type. (**a**) SBEM-based reconstructions and synaptic targets for two orphaned axon segments. Colored spheres mark the locations and types of synapses. (**b**) Axon collaterals (LM-based reconstruction) of an $HVC_{(RA)}$ neuron with branch nodes (gold circles), the soma (black circle), and the HVC border (dashed lines). (**c**) Mean axon length (black) and branch node densities (gold) vs. soma distance (n=15 cells). (**d**) The ratio of synapses onto inhibitory interneurons vs. estimated distance from the soma ($p < 0.005$, Pearson's correlation). (**e**,**f**) The density of synapses onto $HVC_{(RA)}$ (**e**) and $HVC_{(X)}$ (**f**) vs. estimated distance from soma ($p < 0.002$, Pearson's correlation, combining $HVC_{(RA)}$ and $HVC_{(X)}$ values). (**g**) Total synaptic size (summated active zone area, $\mu m^2/mm$) onto excitatory neurons vs. estimated distance of the presynaptic axon from the soma ($p < 0.05$, Pearson's correlation). Vertical error bars: SEM of the Poisson-distribution means estimated from the number of synapses on each axon segment (**e-g**) or the SEM of an assumed underlying binomial count

distribution (**d**). Horizontal error bars from quantiles 0.16 to 0.84 of the distance distribution based on the nearest neighbor sampling approach (see Methods). (**h**) Proposed circuit architecture. $HVC_{(RA)}$ neurons (red) target inhibitory interneurons (blue) proximally and other $HVC_{(RA)}$ neurons distally.

Figure 3—figure supplement 1. Synaptic properties of $HVC_{(RA)}$ axons, using a Bayesian approach to estimate distance from soma. (**a**) Total synaptic strength (summated active zone area/pathlength) onto excitatory neurons vs. estimated distance of the presynaptic axon from the soma ($p < 0.05$, Pearson's correlation). (**b**) The ratio of synapses onto inhibitory interneurons vs. estimated distance from soma ($p < 0.01$, Pearson's correlation). (**c,d**) The density of synapses onto $HVC_{(RA)}$ (**c**) and $HVC_{(X)}$ (**d**) vs. estimated distance from soma ($p < 0.002$, Pearson's correlation, combining $HVC_{(RA)}$ and $HVC_{(X)}$ values). Vertical bars represent the SEM of an assumed underlying Poisson distributed synapse counting process (**a,c,d**) or (**b**) the SEM of an assumed underlying Binomial count distribution. (**a-d**) Horizontal error bars correspond to a 0.16 and 0.84 quantile of the Bayesian posterior distribution, see Methods.

Figure 3—figure supplement 2. A SBEM-based reconstruction and synaptic targets for an orphaned axon with high branch density. Small spheres mark the location of synapses, with the color indicating the target type. Note the higher frequency of inhibitory targets (blue) along the length of the reconstruction compared with other orphaned axons with low branch density (see Figure 3a).

Figure 3—figure supplement 3. A small population of RA neurons project to HVC. (**a**) The borders of RA were traced across nine sequential 100 µm thick sagittal sections, and the location of each retrogradely labeled HVC-projecting RA neuron is marked with a dot. (**b**) DiI injection in HVC resulted in robust retrograde labeling of upstream motor nuclei Uva and NIf, while only a small percentage (< 1%) of cells in RA were labeled (**a**,**c**). An example confocal image of RA is shown in (**c**), revealing a sparse population of retrogradely labeled neurons in the posterior region of the nucleus.

Supplementary Video Legends

Video 1. Video shifting through a z-stack of a sagittal section within HVC, containing a Neurobiotin-filled $HVC_{(RA)}$ neuron stained with DAB. Number of z-sections shown is 144. Voxel size is 92 x 92 x 500nm.

Video 2. Video of a subregion of the acquired SBEM dataset, showing the original data resolution (lossy compression). Number of z-sections shown is 100, translating to 2.9 µm.

Video 3. Video of a subregion of the acquired SBEM dataset, showing a larger field of view with a BDA-labeled $HVC_{(RA)}$ soma (lossy compression). Number of z-sections shown is 200, translating to 5.8 µm.

Video 4. Video of a z-stack of 18 consecutive images (100 x 100 pixels) showing a symmetric synapse. Voxel dimensions: 11 x 11 x 29.

Video 5. Video of a z-stack of 18 consecutive images (100 x 100 pixels) showing an asymmetric synapse. Voxel dimensions: 11 x 11 x 29.

References

Abeles, M. (1991). Corticonics: Neural Circuts of the Cerebral Cortex, Cambridge University Press.

Amador, A., Y. S. Perl, G. B. Mindlin and D. Margoliash (2013). "Elemental gesture dynamics are encoded by song premotor cortical neurons." Nature **495**(7439): 59-64.

Amari, S. (1972). "Learning patterns and pattern sequences by self-organizing nets of threshold elements." IEEE Trans. Comput. **21**: 1197-1206.

Anderson, J. C., R. J. Douglas, K. A. Martin and J. C. Nelson (1994). "Map of the synapses formed with the dendrites of spiny stellate neurons of cat visual cortex." J Comp Neurol **341**(1): 25-38.

Andrasfalvy, B. K., G. L. Galinanes, D. Huber, M. Barbic, J. J. Macklin, K. Susumu, J. B. Delehanty, A. L. Huston, J. K. Makara and I. L. Medintz (2014). "Quantum dot-based multiphoton fluorescent pipettes for targeted neuronal electrophysiology." Nature methods **11**(12): 1237-1241.

Armstrong, E. and H. D. Abarbanel (2016). "Model of the Songbird Nucleus HVC as a Network of Central Pattern Generators." J Neurophysiol: jn 00438 02016.

Aronov, D., A. S. Andalman and M. S. Fee (2008). "A specialized forebrain circuit for vocal babbling in the juvenile songbird." Science **320**(5876): 630-634.

Beaulieu, C., Z. Kisvarday, P. Somogyi, M. Cynader and A. Cowey (1992). "Quantitative distribution of GABA-immunopositive and -immunonegative neurons and synapses in the monkey striate cortex (area 17)." Cereb Cortex **2**(4): 295-309.

Beier, T., C. Pape, N. Rahaman, T. Prange, S. Berg, D. D. Bock, A. Cardona, G. W. Knott, S. M. Plaza, L. K. Scheffer, U. Koethe, A. Kreshuk and F. A. Hamprecht (2017). "Multicut brings automated neurite segmentation closer to human performance." Nat Methods **14**(2): 101-102.

Berning, M., K. M. Boergens and M. Helmstaedter (2015). "SegEM: Efficient Image Analysis for High-Resolution Connectomics." Neuron **87**(6): 1193-1206.

Binas, J., U. Rutishauser, G. Indiveri and M. Pfeiffer (2014). "Learning and stabilization of winner-take-all dynamics through interacting excitatory and inhibitory plasticity." Frontiers in computational neuroscience **8**: 68.

Bock, D. D., W. C. Lee, A. M. Kerlin, M. L. Andermann, G. Hood, A. W. Wetzel, S. Yurgenson, E. R. Soucy, H. S. Kim and R. C. Reid (2011). "Network anatomy and in vivo physiology of visual cortical neurons." Nature **471**(7337): 177-182.

Braitenberg, V. and A. Schüz (1998). Cortex: Statistics and Geometry of Neuronal Connectivity, Springer Berlin Heidelberg.

Budd, J. M., K. Kovacs, A. S. Ferecsko, P. Buzas, U. T. Eysel and Z. F. Kisvarday (2010). "Neocortical axon arbors trade-off material and conduction delay conservation." PLoS computational biology **6**(3): e1000711.

Cannon, J., N. Kopell, T. Gardner and J. Markowitz (2015). "Neural Sequence Generation Using Spatiotemporal Patterns of Inhibition." PLoS Comput Biol **11**(11): e1004581.

Cannon, J., N. Kopell, T. Gardner and J. Markowitz (2015). "Neural Sequence Generation Using Spatiotemporal Patterns of Inhibition." PLoS computational biology **11**(11): e1004581.

Cardin, J. A., J. N. Raksin and M. F. Schmidt (2005). "Sensorimotor nucleus NIf is necessary for auditory processing but not vocal motor output in the avian song system." J Neurophysiol **93**(4): 2157-2166.

Coleman, M. J. and E. T. Vu (2005). "Recovery of impaired songs following unilateral but not bilateral lesions of nucleus uvaeformis of adult zebra finches." J Neurobiol **63**(1): 70-89.

Colonnier, M. (1968). "Synaptic patterns on different cell types in the different laminae of the cat visual cortex. An electron microscope study." Brain research **9**(2): 268-287.

Cragg, B. (1980). "Preservation of extracellular space during fixation of the brain for electron microscopy." Tissue & cell **12**(1): 63-72.

de Wit, J. and A. Ghosh (2016). "Specification of synaptic connectivity by cell surface interactions." Nature reviews. Neuroscience **17**(1): 4.
Denk, W. and H. Horstmann (2004). "Serial block-face scanning electron microscopy to reconstruct three-dimensional tissue nanostructure." PLoS biology **2**(11): e329.
Denk, W. and W. W. Webb (1990). "Optical measurement of picometer displacements of transparent microscopic objects." Applied optics **29**(16): 2382-2391.
Dercksen, V. J., H. C. Hege and M. Oberlaender (2014). "The Filament Editor: an interactive software environment for visualization, proof-editing and analysis of 3D neuron morphology." Neuroinformatics **12**(2): 325-339.
Diesmann, M., M. O. Gewaltig and A. Aertsen (1999). "Stable propagation of synchronous spiking in cortical neural networks." Nature **402**(6761): 529-533.
Dorkenwald, S., P. J. Schubert, M. F. Killinger, G. Urban, S. Mikula, F. Svara and J. Kornfeld (2017). "Automated synaptic connectivity inference for volume electron microscopy." Nat Methods.
Dutar, P., H. M. Vu and D. J. Perkel (1998). "Multiple cell types distinguished by physiological, pharmacological, and anatomic properties in nucleus HVc of the adult zebra finch." Journal of neurophysiology **80**(4): 1828-1838.
Eccles, J. (1976). "From electrical to chemical transmission in the central nervous system." Notes Rec R Soc Lond **30**(2): 219-230.
Egger, R., V. J. Dercksen, D. Udvary, H. C. Hege and M. Oberlaender (2014). "Generation of dense statistical connectomes from sparse morphological data." Frontiers in neuroanatomy **8**: 129.
Euler, T., S. E. Hausselt, D. J. Margolis, T. Breuninger, X. Castell, P. B. Detwiler and W. Denk (2009). "Eyecup scope--optical recordings of light stimulus-evoked fluorescence signals in the retina." Pflugers Archiv : European journal of physiology **457**(6): 1393-1414.
Fee, M. S., A. A. Kozhevnikov and R. H. Hahnloser (2004). "Neural mechanisms of vocal sequence generation in the songbird." Ann N Y Acad Sci **1016**: 153-170.
Fiete, I. R., W. Senn, C. Z. Wang and R. H. Hahnloser (2010). "Spike-time-dependent plasticity and heterosynaptic competition organize networks to produce long scale-free sequences of neural activity." Neuron **65**(4): 563-576.
Gibb, L., T. Q. Gentner and H. D. Abarbanel (2009). "Inhibition and recurrent excitation in a computational model of sparse bursting in song nucleus HVC." Journal of neurophysiology **102**(3): 1748-1762.
Glauert, A. M. and P. R. Lewis (2014). Biological Specimen Preparation for Transmission Electron Microscopy, Princeton University Press.
Goldin, M. A., L. M. Alonso, J. A. Alliende, F. Goller and G. B. Mindlin (2013). "Temperature induced syllable breaking unveils nonlinearly interacting timescales in birdsong motor pathway." PloS one **8**(6): e67814.
Gray, E. G. (1959). "Electron microscopy of synaptic contacts on dendrite spines of the cerebral cortex." Nature **183**(4675): 1592-1593.
Hahnloser, R. H., A. A. Kozhevnikov and M. S. Fee (2002). "An ultra-sparse code underlies the generation of neural sequences in a songbird." Nature **419**(6902): 65-70.
Hamaguchi, K. and R. Mooney (2012). "Recurrent interactions between the input and output of a songbird cortico-basal ganglia pathway are implicated in vocal sequence variability." The Journal of neuroscience : the official journal of the Society for Neuroscience **32**(34): 11671-11687.
Hamaguchi, K., M. Tanaka and R. Mooney (2016). "A Distributed Recurrent Network Contributes to Temporally Precise Vocalizations." Neuron.
Harvey, C. D., P. Coen and D. W. Tank (2012). "Choice-specific sequences in parietal cortex during a virtual-navigation decision task." Nature **484**(7392): 62-68.

Helmstaedter, M. (2013). "Cellular-resolution connectomics: challenges of dense neural circuit reconstruction." Nat Methods **10**(6): 501-507.
Helmstaedter, M., K. L. Briggman and W. Denk (2011). "High-accuracy neurite reconstruction for high-throughput neuroanatomy." Nature neuroscience **14**(8): 1081-1088.
Hopfield, J. J. and D. W. Tank (1985). ""Neural" computation of decisions in optimization problems." Biological cybernetics **52**(3): 141-152.
Januszewski, M., J. Maitin-Shepard, P. Li, J. Kornfeld, W. Denk and V. Jain (2016) "Flood-Filling Networks." ArXiv e-prints **1611**.
Jiang, X., S. Shen, C. R. Cadwell, P. Berens, F. Sinz, A. S. Ecker, S. Patel and A. S. Tolias (2015). "Principles of connectivity among morphologically defined cell types in adult neocortex." Science **350**(6264): aac9462.
Jin, D. Z., F. M. Ramazanoglu and H. S. Seung (2007). "Intrinsic bursting enhances the robustness of a neural network model of sequence generation by avian brain area HVC." Journal of computational neuroscience **23**(3): 283-299.
Karnovsky, M. J. (1971). "Use of ferrocyanide-reduced osmium tetroxide in electron microscopy." Proc 11th Annu Mtg Am Soc Cell Biol.: 146.
Karsh, B. (2016). Alignment Projects. Github. https://github.com/billkarsh/Alignment_Projects. **cf05957**
Kasthuri, N., K. J. Hayworth, D. R. Berger, R. L. Schalek, J. A. Conchello, S. Knowles-Barley, D. Lee, A. Vazquez-Reina, V. Kaynig, T. R. Jones, M. Roberts, J. L. Morgan, J. C. Tapia, H. S. Seung, W. G. Roncal, J. T. Vogelstein, R. Burns, D. L. Sussman, C. E. Priebe, H. Pfister and J. W. Lichtman (2015). "Saturated Reconstruction of a Volume of Neocortex." Cell **162**(3): 648-661.
Komai, S., W. Denk, P. Osten, M. Brecht and T. W. Margrie (2006). "Two-photon targeted patching (TPTP) in vivo." Nature protocols **1**(2): 647-652.
Kornfeld, J. (2017). HVC paper. Github. https://github.com/jmrk84/HVC_paper. **3bd6758**.
Kornfeld, J. (2017). Knossos project. Github. https://github.com/knossos-project/knossos_utils. **010778d**.
Kosche, G., D. Vallentin and M. A. Long (2015). "Interplay of inhibition and excitation shapes a premotor neural sequence." The Journal of neuroscience : the official journal of the Society for Neuroscience **35**(3): 1217-1227.
Kozhevnikov, A. A. and M. S. Fee (2007). "Singing-related activity of identified HVC neurons in the zebra finch." J Neurophysiol **97**(6): 4271-4283.
Kubota, M. and I. Taniguchi (1998). "Electrophysiological characteristics of classes of neuron in the HVc of the zebra finch." Journal of neurophysiology **80**(2): 914-923.
Li, M. and H. Greenside (2006). "Stable propagation of a burst through a one-dimensional homogeneous excitatory chain model of songbird nucleus HVC." Phys Rev E Stat Nonlin Soft Matter Phys **74**(1 Pt 1): 011918.
Long, M. A. and M. S. Fee (2008). "Using temperature to analyse temporal dynamics in the songbird motor pathway." Nature **456**(7219): 189-194.
Long, M. A., D. Z. Jin and M. S. Fee (2010). "Support for a synaptic chain model of neuronal sequence generation." Nature **468**(7322): 394-399.
Lundqvist, M., J. Rose, P. Herman, S. L. Brincat, T. J. Buschman and E. K. Miller (2016). "Gamma and Beta Bursts Underlie Working Memory." Neuron.
Lynch, G. F., T. S. Okubo, A. Hanuschkin, R. H. Hahnloser and M. S. Fee (2016). "Rhythmic Continuous-Time Coding in the Songbird Analog of Vocal Motor Cortex." Neuron **90**(4): 877-892.
Markowitz, J. E., W. A. Liberti, 3rd, G. Guitchounts, T. Velho, C. Lois and T. J. Gardner (2015). "Mesoscopic patterns of neural activity support songbird cortical sequences." PLoS Biol **13**(6): e1002158.

McGuire, B. A., C. D. Gilbert, P. K. Rivlin and T. N. Wiesel (1991). "Targets of horizontal connections in macaque primary visual cortex." J Comp Neurol **305**(3): 370-392.
Mello, G. B., S. Soares and J. J. Paton (2015). "A scalable population code for time in the striatum." Current biology : CB **25**(9): 1113-1122.
Mooney, R. (2000). "Different subthreshold mechanisms underlie song selectivity in identified HVc neurons of the zebra finch." The Journal of neuroscience : the official journal of the Society for Neuroscience **20**(14): 5420-5436.
Mooney, R. and J. F. Prather (2005). "The HVC microcircuit: the synaptic basis for interactions between song motor and vocal plasticity pathways." The Journal of neuroscience : the official journal of the Society for Neuroscience **25**(8): 1952-1964.
Mostafa, H. and G. Indiveri (2014). "Sequential activity in asymmetrically coupled winner-take-all circuits." Neural computation **26**(9): 1973-2004.
Narayanan, R. T., R. Egger, A. S. Johnson, H. D. Mansvelder, B. Sakmann, C. P. de Kock and M. Oberlaender (2015). "Beyond Columnar Organization: Cell Type- and Target Layer-Specific Principles of Horizontal Axon Projection Patterns in Rat Vibrissal Cortex." Cerebral cortex **25**(11): 4450-4468.
Nixdorf-Bergweiler, B. and H.-J. Bischof (2007). A Stereotaxic Atlas Of The Brain Of The Zebra Finch, Taeniopygia Guttata. Bethesda, MD, National Center for Biotechnology Information (US).
Nottebohm, F., D. B. Kelley and J. A. Paton (1982). "Connections of vocal control nuclei in the canary telencephalon." The Journal of comparative neurology **207**(4): 344-357.
Nottebohm, F., T. M. Stokes and C. M. Leonard (1976). "Central control of song in the canary, Serinus canarius." The Journal of comparative neurology **165**(4): 457-486.
Oberlaender, M., P. J. Broser, B. Sakmann and S. Hippler (2009). "Shack-Hartmann wave front measurements in cortical tissue for deconvolution of large three-dimensional mosaic transmitted light brightfield micrographs." Journal of microscopy **233**(2): 275-289.
Oberlaender, M., R. M. Bruno, B. Sakmann and P. J. Broser (2007). "Transmitted light brightfield mosaic microscopy for three-dimensional tracing of single neuron morphology." Journal of biomedical optics **12**(6): 064029.
Pastalkova, E., V. Itskov, A. Amarasingham and G. Buzsaki (2008). "Internally generated cell assembly sequences in the rat hippocampus." Science **321**(5894): 1322-1327.
Peters, A. (2002). "Examining neocortical circuits: some background and facts." J Neurocytol **31**(3-5): 183-193.
Peters, A. J., S. X. Chen and T. Komiyama (2014). "Emergence of reproducible spatiotemporal activity during motor learning." Nature **510**(7504): 263-267.
Picardo, M. A., J. Merel, K. A. Katlowitz, D. Vallentin, D. E. Okobi, S. E. Benezra, R. C. Clary, E. A. Pnevmatikakis, L. Paninski and M. A. Long (2016). "Population-Level Representation of a Temporal Sequence Underlying Song Production in the Zebra Finch." Neuron **90**(4): 866-876.
Pinault, D. (1996). "A novel single-cell staining procedure performed in vivo under electrophysiological control: morpho-functional features of juxtacellularly labeled thalamic cells and other central neurons with biocytin or Neurobiotin." Journal of neuroscience methods **65**(2): 113-136.
Pologruto, T. A., B. L. Sabatini and K. Svoboda (2003). "ScanImage: flexible software for operating laser scanning microscopes." Biomedical engineering online **2**: 13.
Rajan, K., C. D. Harvey and D. W. Tank (2016). "Recurrent Network Models of Sequence Generation and Memory." Neuron.
Rees, C. L., K. Moradi and G. A. Ascoli (2017). "Weighing the Evidence in Peters' Rule: Does Neuronal Morphology Predict Connectivity?" Trends Neurosci **40**(2): 63-71.
Reiner, A., C. L. Veenman, L. Medina, Y. Jiao, N. Del Mar and M. G. Honig (2000). "Pathway tracing using biotinylated dextran amines." J Neurosci Methods **103**(1): 23-37.

Roberts, T. F., M. E. Klein, M. F. Kubke, J. M. Wild and R. Mooney (2008). "Telencephalic neurons monosynaptically link brainstem and forebrain premotor networks necessary for song." J Neurosci **28**(13): 3479-3489.
Schalek, R. L., D. Lee, N. Kasthuri, A. Peleg, T. Jones, V. Kaynig, D. Haehn, H. Pfister, D. Cox and J. W. Lichtman (2016). "Imaging a 1 mm^3 Volume of Rat Cortex Using a MultiBeam SEM." Microsc. Microanal. **22**(Supp 3): 582-583.
Scharff, C., J. R. Kirn, M. Grossman, J. D. Macklis and F. Nottebohm (2000). "Targeted neuronal death affects neuronal replacement and vocal behavior in adult songbirds." Neuron **25**(2): 481-492.
Scheffer, L. K., B. Karsh and S. Vitaladevun (2013). "Automated Alignment of Imperfect EM Images for Neural Reconstruction." arXiv https://arxiv.org/abs/1304.6034.
Scott, B. B., T. Gardner, N. Ji, M. S. Fee and C. Lois (2012). "Wandering neuronal migration in the postnatal vertebrate forebrain." J Neurosci **32**(4): 1436-1446.
Seligman, A. M., H. L. Wasserkrug and J. S. Hanker (1966). "A new staining method (OTO) for enhancing contrast of lipid--containing membranes and droplets in osmium tetroxide--fixed tissue with osmiophilic thiocarbohydrazide(TCH)." The Journal of cell biology **30**(2): 424-432.
Seung, H. S. (2009). "Reading the book of memory: sparse sampling versus dense mapping of connectomes." Neuron **62**(1): 17-29.
Sholl, D. A. (1953). "Dendritic organization in the neurons of the visual and motor cortices of the cat." Journal of anatomy **87**(4): 387-406.
Stepanyants, A., L. M. Martinez, A. S. Ferecsko and Z. F. Kisvarday (2009). "The fractions of short- and long-range connections in the visual cortex." Proceedings of the National Academy of Sciences of the United States of America **106**(9): 3555-3560.
Usher, M. and J. L. McClelland (2001). "The time course of perceptual choice: the leaky, competing accumulator model." Psychological review **108**(3): 550-592.
Vallentin, D. and M. A. Long (2015). "Motor origin of precise synaptic inputs onto forebrain neurons driving a skilled behavior." J Neurosci **35**(1): 299-307.
Vu, E. T., M. E. Mazurek and Y. C. Kuo (1994). "Identification of a forebrain motor programming network for the learned song of zebra finches." The Journal of neuroscience : the official journal of the Society for Neuroscience **14**(11 Pt 2): 6924-6934.
Walton, J. (1979). "Lead asparate, an en bloc contrast stain particularly useful for ultrastructural enzymology." The journal of histochemistry and cytochemistry : official journal of the Histochemistry Society **27**(10): 1337-1342.
Wang, N., P. Hurley, C. Pytte and J. R. Kirn (2002). "Vocal control neuron incorporation decreases with age in the adult zebra finch." J Neurosci **22**(24): 10864-10870.
Wild, J. M., M. N. Williams, G. J. Howie and R. Mooney (2005). "Calcium-binding proteins define interneurons in HVC of the zebra finch (Taeniopygia guttata)." The Journal of comparative neurology **483**(1): 76-90.
Yildiz, I. B. and S. J. Kiebel (2011). "A hierarchical neuronal model for generation and online recognition of birdsongs." PLoS computational biology **7**(12): e1002303.

Figure 1

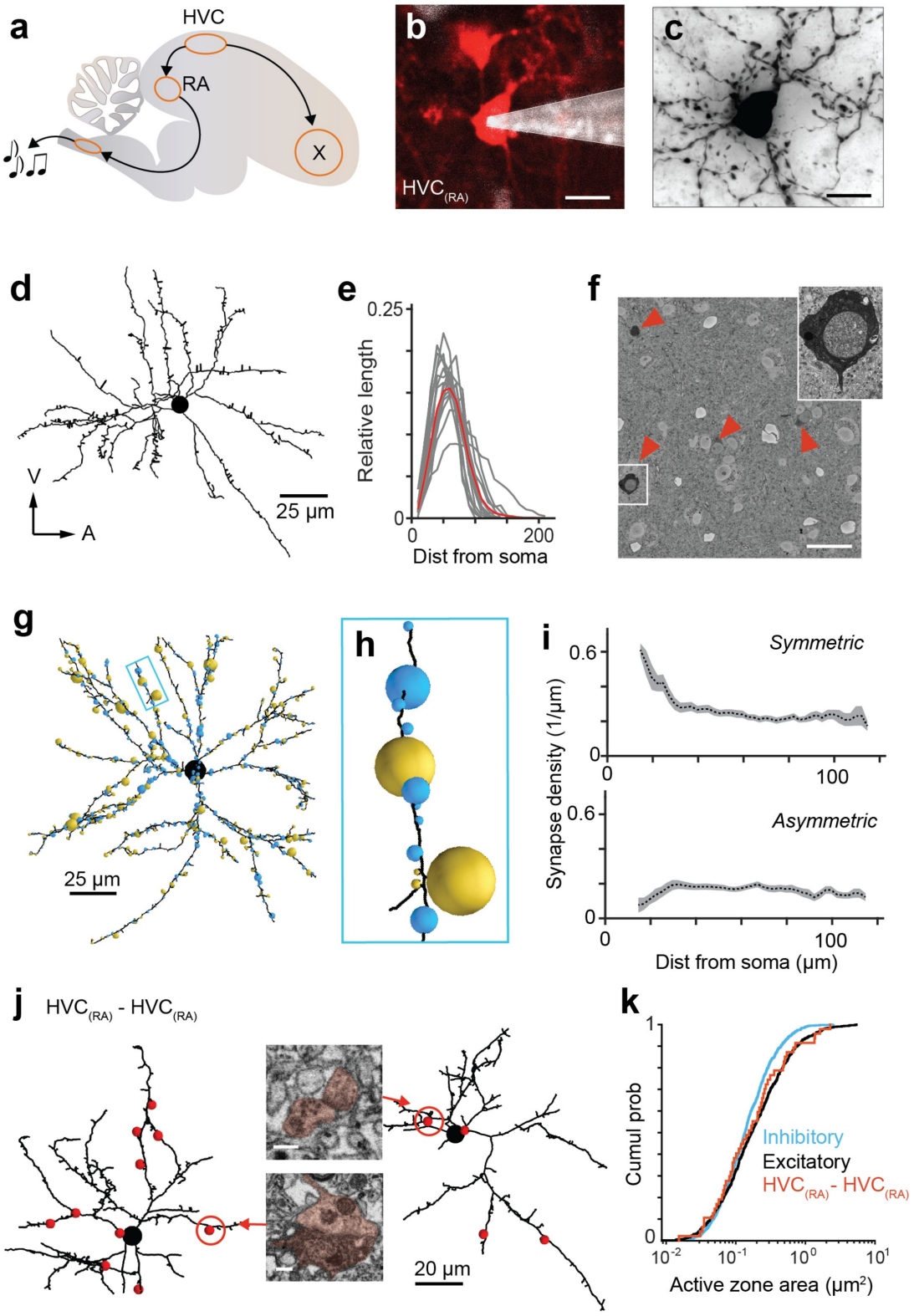
a
HVC
RA
X
b
HVC(RA)
c
d
V
A
25 µm
e
0.25
Relative length
0
0
200
Dist from soma
f
g
25 µm
h
i
Symmetric
0.6
0
0
100
Asymmetric
0.6
0
0
100
Synapse density (1/µm)
Dist from soma (µm)
j
HVC(RA) - HVC(RA)
20 µm
k
1
0
Cumul prob
Inhibitory
Excitatory
HVC(RA) - HVC(RA)
10-2
10-1
100
101
Active zone area (µm2)

Figure 1 - supplement 1

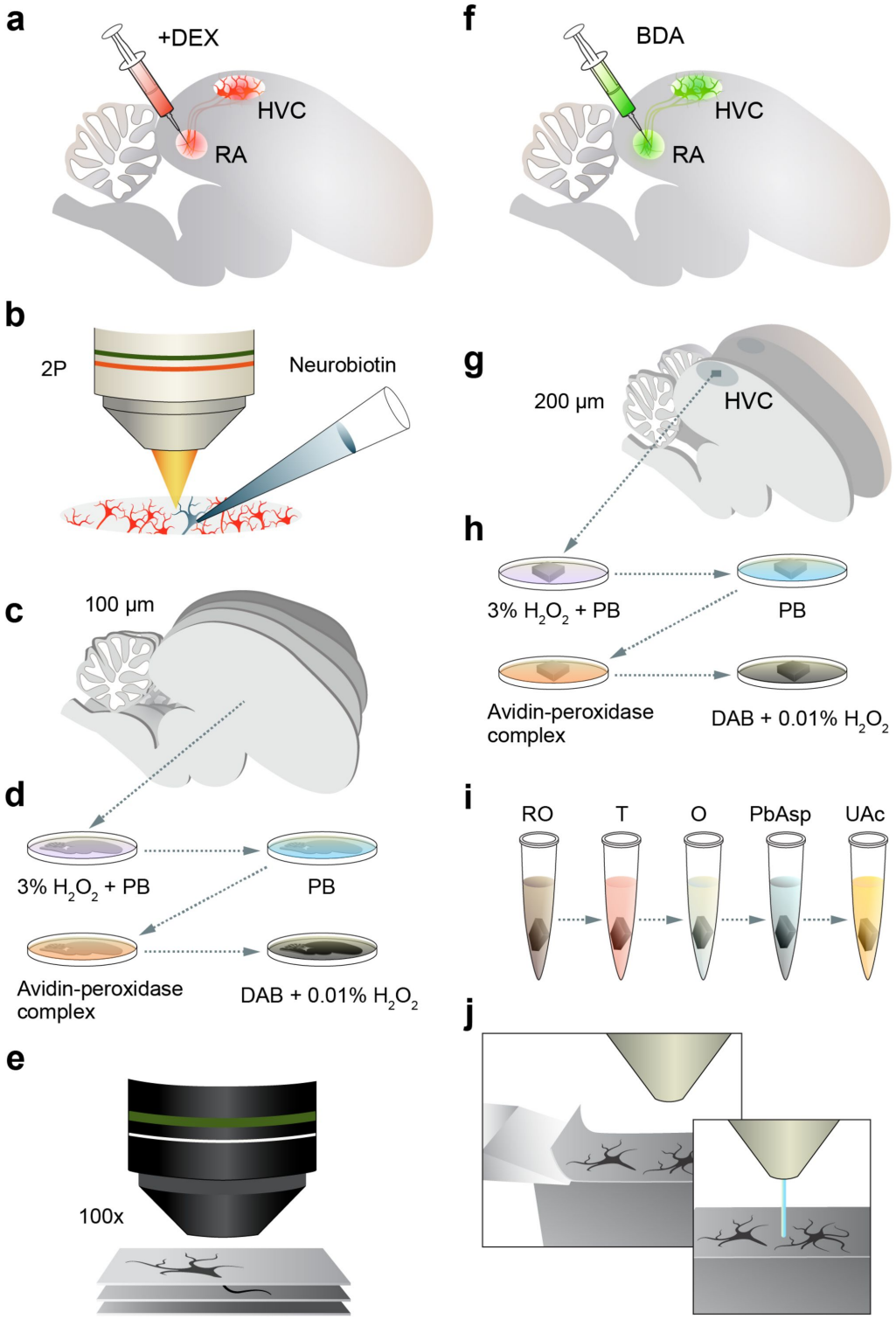

Figure 1 - supplement 2

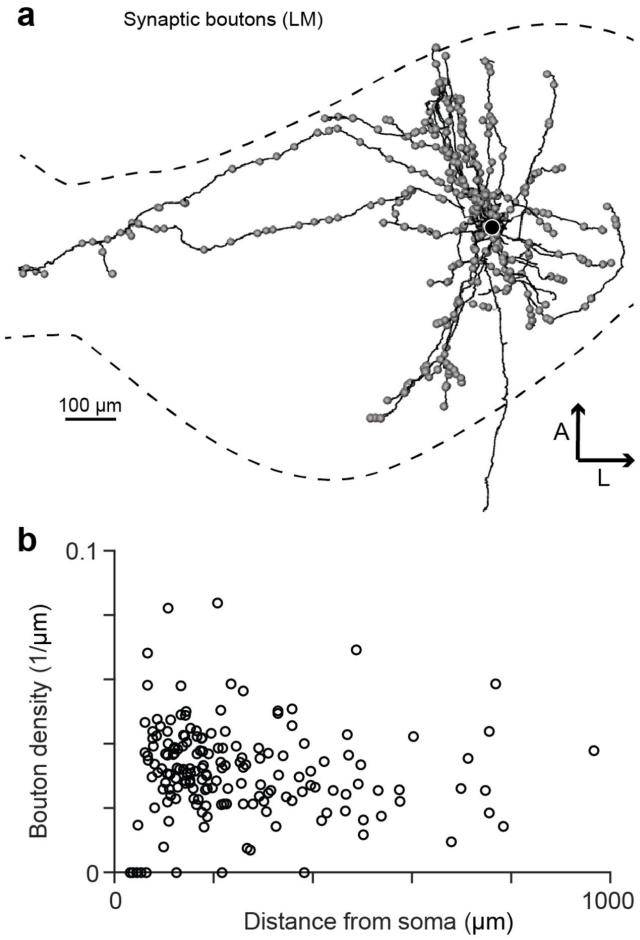

Figure 1 - supplement 3

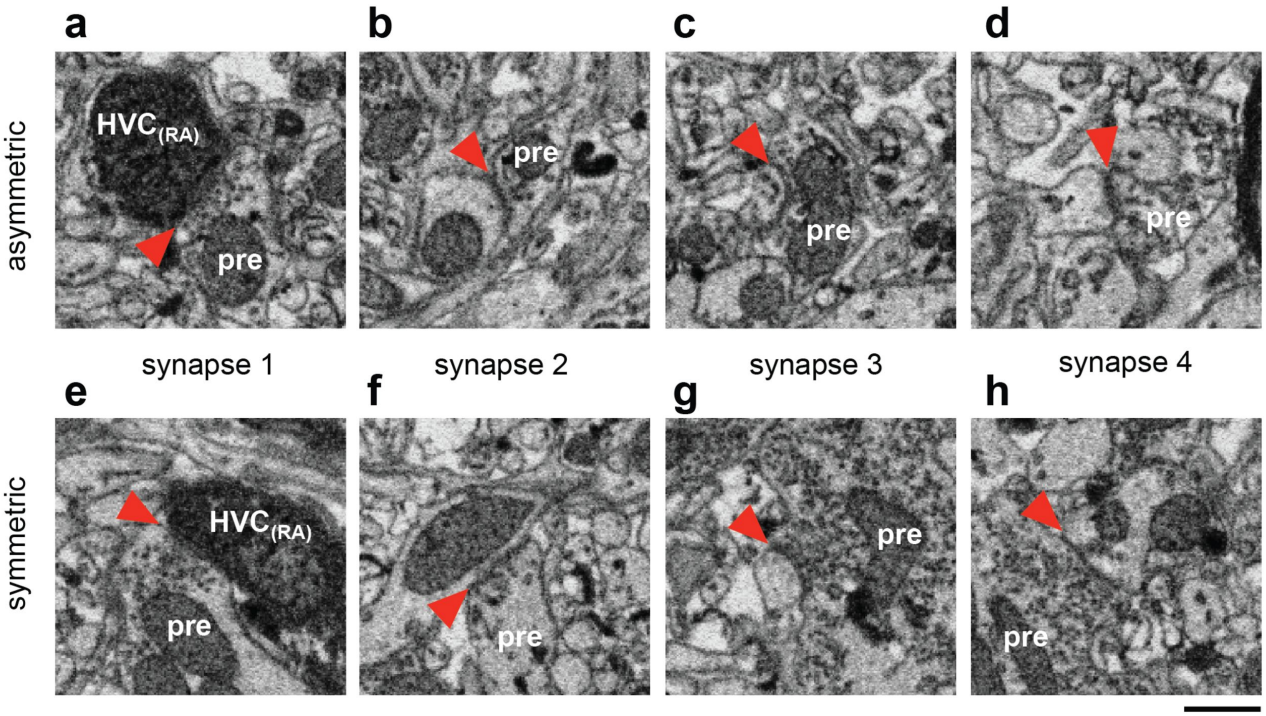

Figure 1 - supplement 4

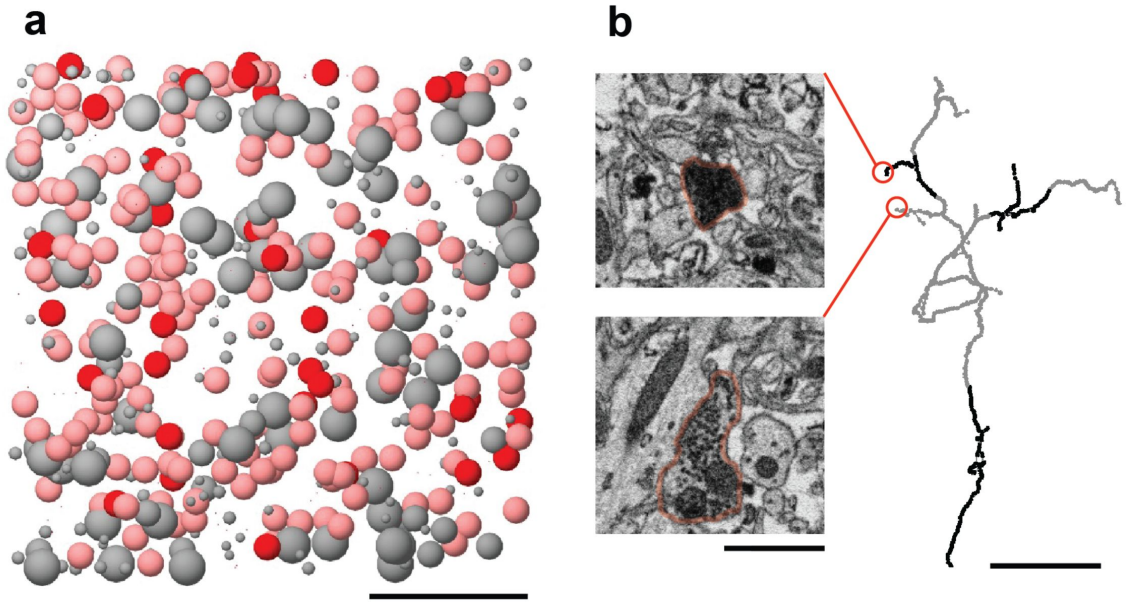

Figure 2

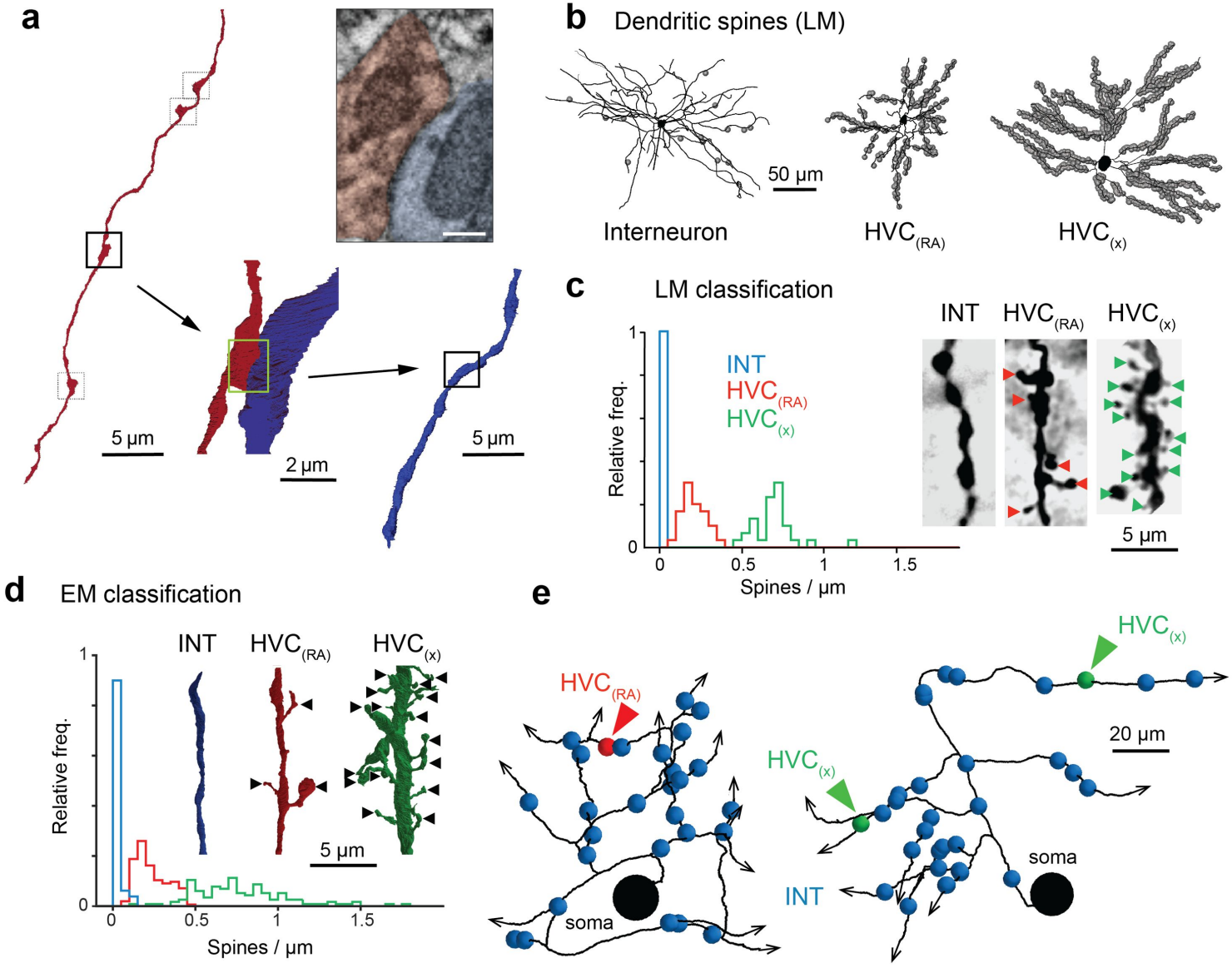
a
5 µm
2 µm
5 µm
b
Dendritic spines (LM)
50 µm
Interneuron
HVC(RA)
HVC(x)
c
LM classification
INT
HVC(RA)
HVC(x)
Relative freq.
Spines / µm
5 µm
d
EM classification
INT
HVC(RA)
HVC(x)
Relative freq.
Spines / µm
5 µm
e
HVC(RA)
HVC(x)
soma
HVC(x)
20 µm
INT
soma

Figure 2 - supplement 1

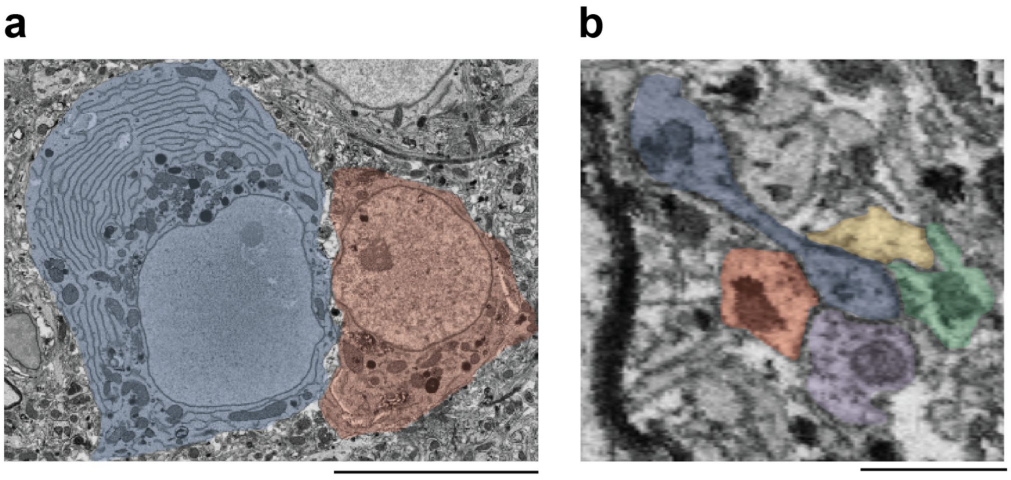

Figure 3

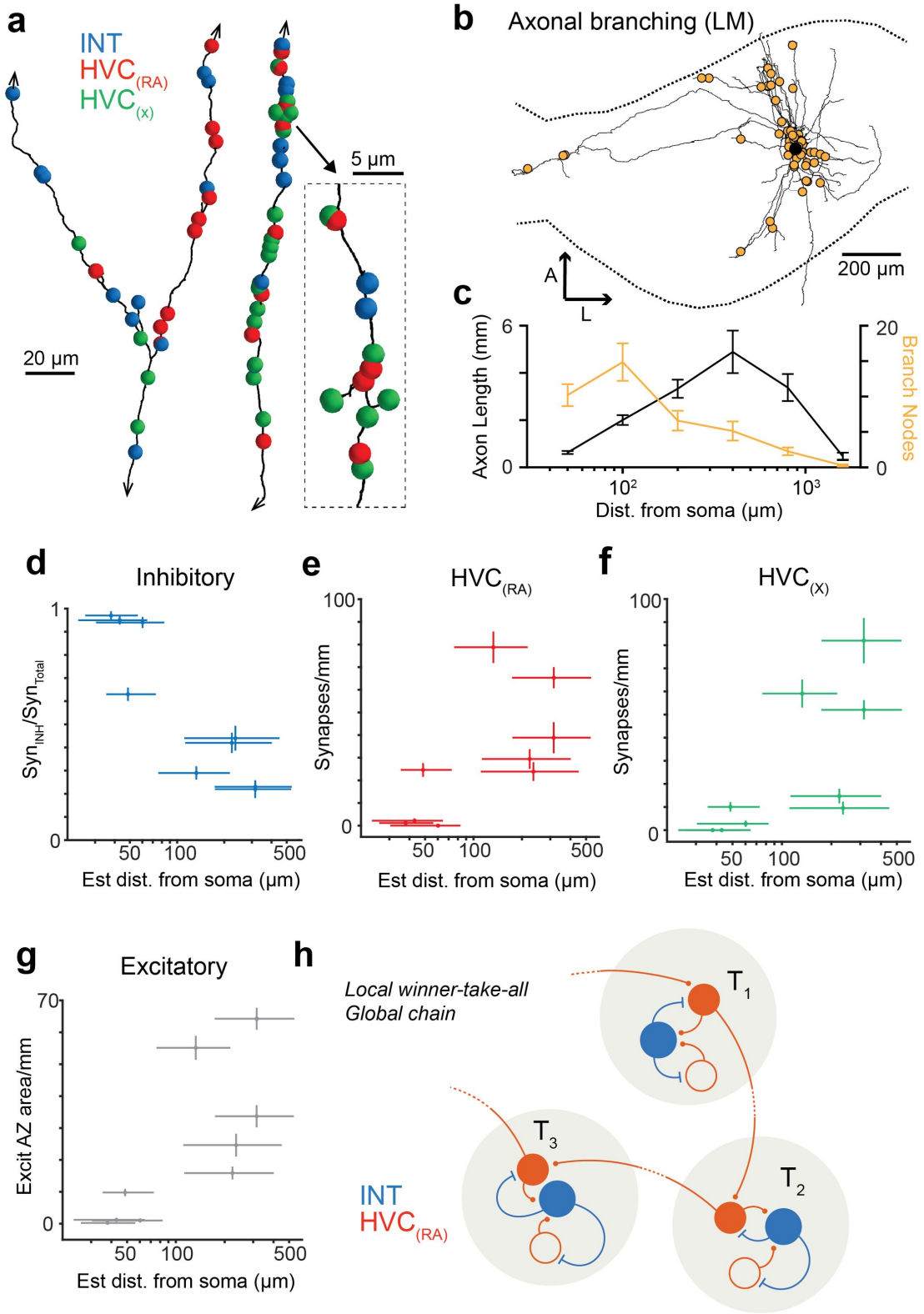
a
INT
HVC(RA)
HVC(x)
5 µm
20 µm
b
Axonal branching (LM)
A
L
200 µm
c
Axon Length (mm)
Branch Nodes
Dist. from soma (µm)
d
Inhibitory
Syn_INH/Syn_Total
Est dist. from soma (µm)
e
HVC(RA)
Synapses/mm
Est dist. from soma (µm)
f
HVC(X)
Synapses/mm
Est dist. from soma (µm)
g
Excitatory
Excit AZ area/mm
Est dist. from soma (µm)
h
Local winner-take-all
Global chain
T1
T2
T3
INT
HVC(RA)

Figure 3 - supplement 1

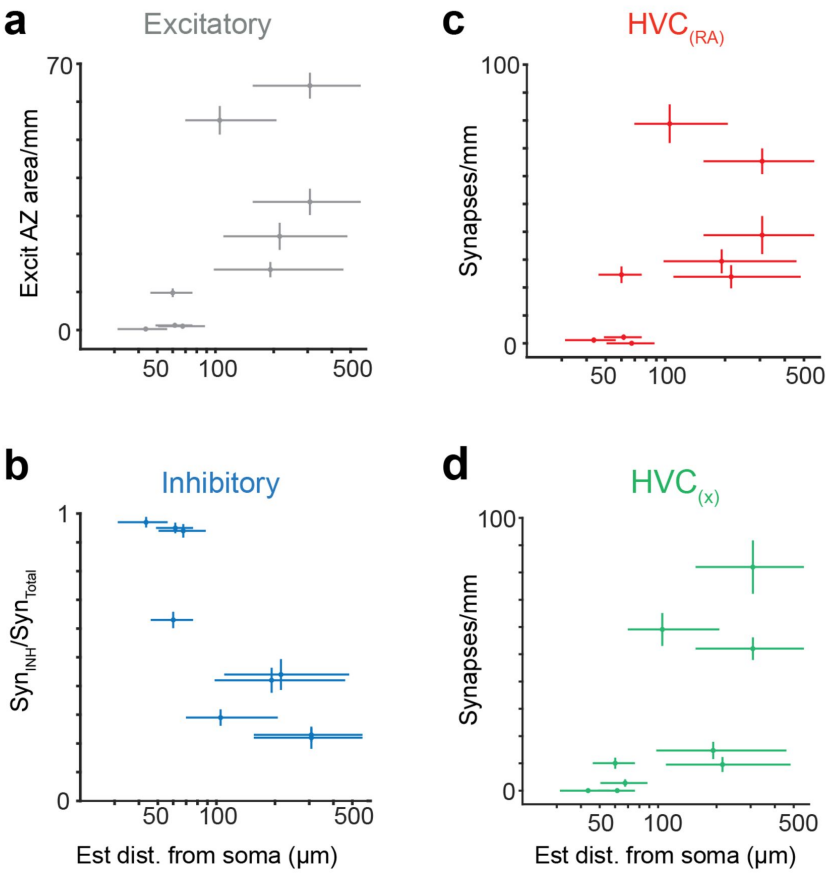

Figure 3 - supplement 2

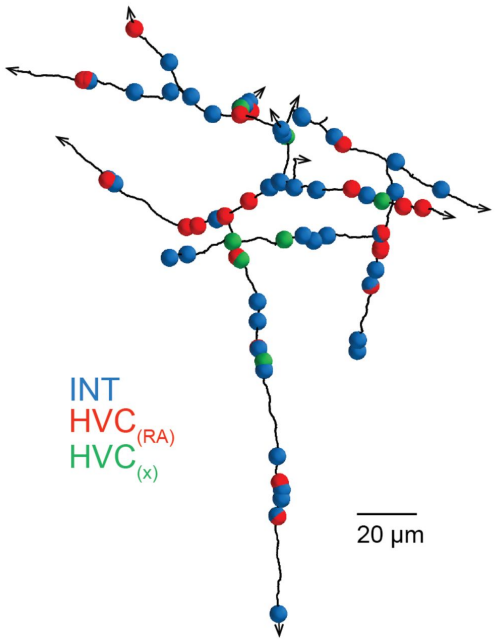

Figure 3 - supplement 3